Evidence for the Operation of the Hanle and Magneto-Optical Effects in the Scattering Polarization Signals Observed by CLASP2 Across the Mg II h & k Lines

Ryohko Ishikawa,[1] Javier Trujillo Bueno,[2, 3, 4] Ernest Alsina Ballester,[2, 3] Luca Belluzzi,[5, 6, 7]
Tanausú del Pino Alemán,[2, 3] David E. McKenzie,[8] Frédéric Auchère,[9] Ken Kobayashi,[8] Takenori J. Okamoto,[1]
Laurel A. Rachmeler,[10] and Donguk Song[11, 1]

[1]National Astronomical Observatory of Japan,
2-21-1 Osawa, Mitaka, Tokyo 181-8588 Japan
[2]Instituto de Astrofísica de Canarias, E-38205 La Laguna, Tenerife, Spain
[3]Departamento de Astrofísica, Universidad de La Laguna, E-38206 La Laguna, Tenerife, Spain
[4]Consejo Superior de Investigaciones Científicas, Spain
[5]IRSOL Istituto Ricerche Solari "Aldo e Cele Daccò", Università della Svizzera italiana (USI),
CH-6605 Locarno-Monti, Switzerland
[6]Leibniz-Institut für Sonnenphysik (KIS), D-79104 Freiburg, Germany
[7]Euler Institute, Università della Svizzera italiana (USI), CH-6900 Lugano, Switzerland
[8]NASA Marshall Space Flight Center, Huntsville, AL 35812, USA
[9]Institut d'Astrophysique Spatiale, 91405 Orsay Cedex, France
[10]National Oceanic and Atmospheric Administration,
National Centers for Environmental Information, Boulder, CO 80305, USA
[11]Korea Astronomy and Space Science Institute 776,
Daedeokdae-ro, Yuseong-gu, Daejeon 305-348, Republic of Korea

ABSTRACT

Radiative transfer investigations of the solar Mg II h & k resonance lines around 280 nm showed that, while their circular polarization (Stokes V) signals arise from the Zeeman effect, the linear polarization profiles (Stokes Q and U) are dominated by the scattering of anisotropic radiation and the Hanle and magneto-optical (MO) effects. Using the unprecedented observations of the Mg II and Mn I resonance lines obtained by the Chromospheric LAyer Spectro-Polarimeter (CLASP2), here we investigate how the linear polarization signals at different wavelengths (i.e., at the center, and at the near and far wings of the k line) vary with the longitudinal component of the magnetic field (B_L) at their approximate height of formation. The B_L is estimated from the V signals in the aforementioned spectral lines. Particular attention is given to the following quantities that are expected to be influenced by the presence of magnetic fields through the Hanle and MO effects: the sign of the U signals, the total linear polarization amplitude (LP) and its direction (χ) with respect to a reference direction. We find that at the center and near wings of the k line, the behavior of these quantities is significantly different in the observed quiet and plage regions, and that both LP and χ seem to depend on B_L. These observational results are indicative of the operation of the Hanle effect at the center of the k line and of the MO effects at the near wings of the k line.

1. INTRODUCTION

The remote sensing inference of the magnetic fields that permeate the solar atmosphere is crucial to under-

Corresponding author: Ryohko Ishikawa
ryoko.ishikawa@nao.ac.jp

arXiv:2302.03303v1 [astro-ph.SR] 7 Feb 2023

stand the energy transfer from the photosphere to the chromosphere and corona, and its dissipation. Over the last decades we have achieved increasingly better determinations of the photospheric magnetic fields (e.g., Bellot Rubio & Orozco Suárez 2019). However, there is a serious lack of empirical information on the chromosphere and the layers above, where the magnetic field dominates the dynamics, structuring, and heating of the plasma.

Over the last ten years, a series of theoretical investigations pointed out that the scattering of anisotropic radiation and the Hanle and Zeeman effects should produce measurable polarization signals in several ultraviolet (UV) spectral lines, such as hydrogen Lyman-α at 121.6 nm and Mg II h & k around 280 nm, which encode information on the outer layers of the solar chromosphere (see the review by Trujillo Bueno et al. 2017). The Hanle effect is the magnetically induced modification of the linear polarization produced by scattering processes (i.e., scattering polarization) at the center of a spectral line (Landi Degl'Innocenti & Landolfi 2004). Radiative transfer (RT) calculations in one-dimensional (1D) models of the solar atmosphere show that the observational signatures found at lines of sight away from the solar disk center are the depolarization and rotation of the plane of linear polarization (Trujillo Bueno et al. 2011; del Pino Alemán et al. 2016; Alsina Ballester et al. 2016). However, the line-center scattering polarization is also strongly influenced by the vertical stratification of the atmosphere and the lack of axial symmetry of the incident radiation field (i.e., the radiation illuminating each point within the medium). The former influence causes the amplitudes of the scattering polarization to be different for different atmospheric models (Trujillo Bueno et al. 2017; del Pino Alemán et al. 2020). The latter can be due to the horizontal inhomogeneities of the solar atmosphere (temperature and density variations) and to the gradients of the plasma macroscopic velocity (Manso Sainz & Trujillo Bueno 2011; Štěpán et al. 2015; Štěpán & Trujillo Bueno 2016; Jaume Bestard et al. 2021). For this reason, inferring the chromospheric magnetic field via the Hanle effect is not straightforward. The same applies to the scattering linear polarization signals in the wings of hydrogen Lyman-α and Mg II h & k. Via the magneto-optical (MO) terms of the Stokes-vector transfer equation (see Eq. 6.85 in Landi Degl'Innocenti & Landolfi 2004) these wing polarization signals are sensitive to the presence of magnetic fields in their region of formation (del Pino Alemán et al. 2016; Alsina Ballester et al. 2016, 2019; del Pino Alemán et al. 2020). These wing

polarization signals are also affected by the above-mentioned vertical stratification and the lack of axial symmetry.

The theoretical studies mentioned above led to the development of a series of sounding rocket experiments: the Chromospheric Lyman-Alpha Spectro-Polarimeter (hereafter CLASP1) and the Chromospheric LAyer Spectro-Polarimeter (CLASP2), whose aim was to demonstrate that UV spectropolarimetry is a suitable technique to determine the magnetic field in the upper chromosphere and the transition region.

In 2015, CLASP1 provided the first measurements of the linear polarization signals (i.e., the Stokes Q and U parameters)[1] produced by scattering processes in the hydrogen Lyman-α line (Kano et al. 2017). The Hanle effect operates at the spectral line center and for the hydrogen Lyman-α line the Hanle critical magnetic field strength is 53 G. A detailed analysis of the intensity (Stokes I) and the fractional linear polarization (Q/I and U/I) profiles observed by CLASP1 close to the limb (see Ishikawa et al. 2017) revealed that the U/I signals in the wings of the hydrogen Lyman-α line, where the Hanle effect does not operate, always changed their sign when crossing the center of four bright structures whose photospheric magnetic flux was measured by the Solar Dynamic Observatory (SDO, Pesnell et al. 2012). These bright structures were also identified at the center of the Lyman-α intensity profiles. However, at the Lyman-α line center, such a change of sign in U/I was found only in an inter-network bright structure, where the photospheric magnetic flux was found to be relatively low, but not in the aforementioned network and enhanced network bright structures, where the photospheric magnetic flux was found to be larger. On the basis of the idealized polarization maps obtained by Štěpán & Trujillo Bueno (2012) with and without magnetic fields in a very simple 3D model of the solar atmosphere (see also Figure 7 of Ishikawa et al. 2017), the above-mentioned curious behavior of the observed Lyman-α U/I signals was taken as evidence for the operation of the Hanle effect at the center of the Lyman-α line (Ishikawa et al. 2017). We note that it remains to be clarified why the U/I wing signals always changed their sign when crossing the center of such bright structures irrespective of their magnetic flux given that, via the MO terms of the Stokes-vector transfer equation, the wings of the Q/I and U/I profiles of the hydrogen Lyman-α line are indeed sensitive to the presence of magnetic fields with strengths similar

---

[1] In this paper, the reference direction for positive Stokes Q is the parallel to the nearest solar limb.

to those that produce the Hanle effect at the line center (see Alsina Ballester et al. 2019).

In 2019, CLASP2 provided the first ever spectrally and spatially resolved Stokes profiles observations (intensity I, linear polarization Q and U, and circular polarization V) across the Mg II h & k lines, in an active region plage and in a quiet region near the solar limb. The Zeeman-induced Stokes V circular polarization signals were detected in several UV spectral lines, and in particular in the Mg II h & k lines and in the nearby Mn I resonance lines. The amplitude of these V/I signals was significant in the observed active region plage and in the surrounding enhanced network. By applying the weak field approximation (WFA), Ishikawa et al. (2021) could determine the longitudinal component (B_L) of the magnetic field from the bottom to the top of the chromosphere, both in the plage and in the surrounding enhanced network features.

CLASP2 measured the linear polarization across the Mg II h & k lines in both quiet Sun and plage targets. The Q/I and U/I profiles are dominated by the scattering of anisotropic radiation in the Mg II h & k lines, the modeling of which requires taking into account the joint action of partial frequency redistribution (PRD) and quantum interference between the upper $J-$levels of these lines (Belluzzi & Trujillo Bueno 2012). The presence of a magnetic field produces measurable modifications of the scattering polarization over a wide wavelength range across the Mg II h & k lines (del Pino Alemán et al. 2016; Alsina Ballester et al. 2016). Via the Hanle effect, the Q/I and U/I line center signals of the k line are sensitive to the strength, between approximately 5 and 125 G,[2] as well as to the orientation of the magnetic fields present in the upper chromosphere. For stronger fields the Hanle effect is in its saturation regime and the line center signals are only sensitive to the orientation of the magnetic field. Moreover, the MO terms of the Stokes-vector transfer equation introduce magnetic sensitivity in the wings of the Mg II h & k lines (Alsina Ballester et al. 2016; del Pino Alemán et al. 2016). Magnetic fields as weak as those capable of producing the Hanle effect in the k line (see above) are sufficient to significantly affect the polarization wings of these lines via the MO effects. The typical observational signatures of the MO effects are a depolarization of the Q/I wing signals and the appearance of U/I wing signals. Equivalently, they are characterized by a decrease of the linear polarization degree

---

[2] The Hanle critical field strength is 25 G for the k line.

and a rotation of the plane of linear polarization (e.g., see Figure 4 of Alsina Ballester et al. 2016).

By combining the information provided by the Zeeman-induced circular polarization in the Mg II h & k lines and the linear polarization resulting from the joint action of scattering processes and the Hanle and the MO effects, we can aim at determining the magnetic field vector. To this end, it is first important to identify the observational signature of the Hanle and MO effects in the CLASP2 data. In a recent paper we demonstrated that the Q/I and U/I patterns observed by CLASP2 across the Mg II h & k lines are indeed caused by the scattering of anisotropic radiation, with PRD and J-state interference playing a key role (Rachmeler et al. 2022). In this paper, we aim at providing observational evidence of the operation of the Hanle effect in the core of the k line and of the MO effects in the wings of the Mg II h & k lines.

2. OBSERVATIONS AND DATA REDUCTION
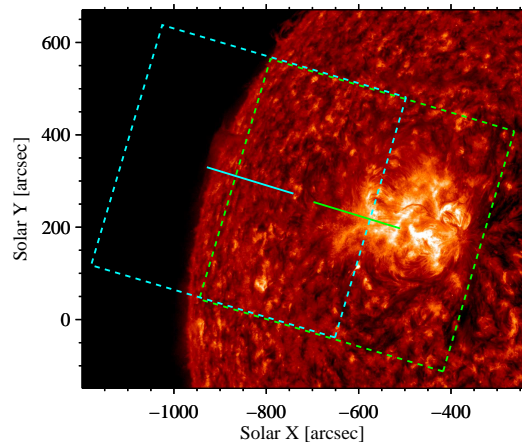
Figure 1. SDO/AIA 30.4 nm intensity image temporally averaged between 16:53:41 and 16:58:41 UT on 2019 April 11. Cyan and green boxes in dashed lines indicate the CLASP2/SJ fields of view for the limb and plage targets, respectively. The solid line at the center of each box indicates the CLASP2 spectrograph slit position for each target.

On 11 April 2019, CLASP2 conducted sit-and-stare observations at three positions on the solar disk. The first target, observed during 15 s, was the solar disk center. This observation allowed verifying that the instrumental polarization is negligible, roughly two orders of magnitude smaller than our required polarization accuracy of 0.1% (Song et al. 2022). The second target was the East side of the NOAA 12738 active region (hereafter, plage target, see green box in Fig. 1) observed from

plage target

limb target
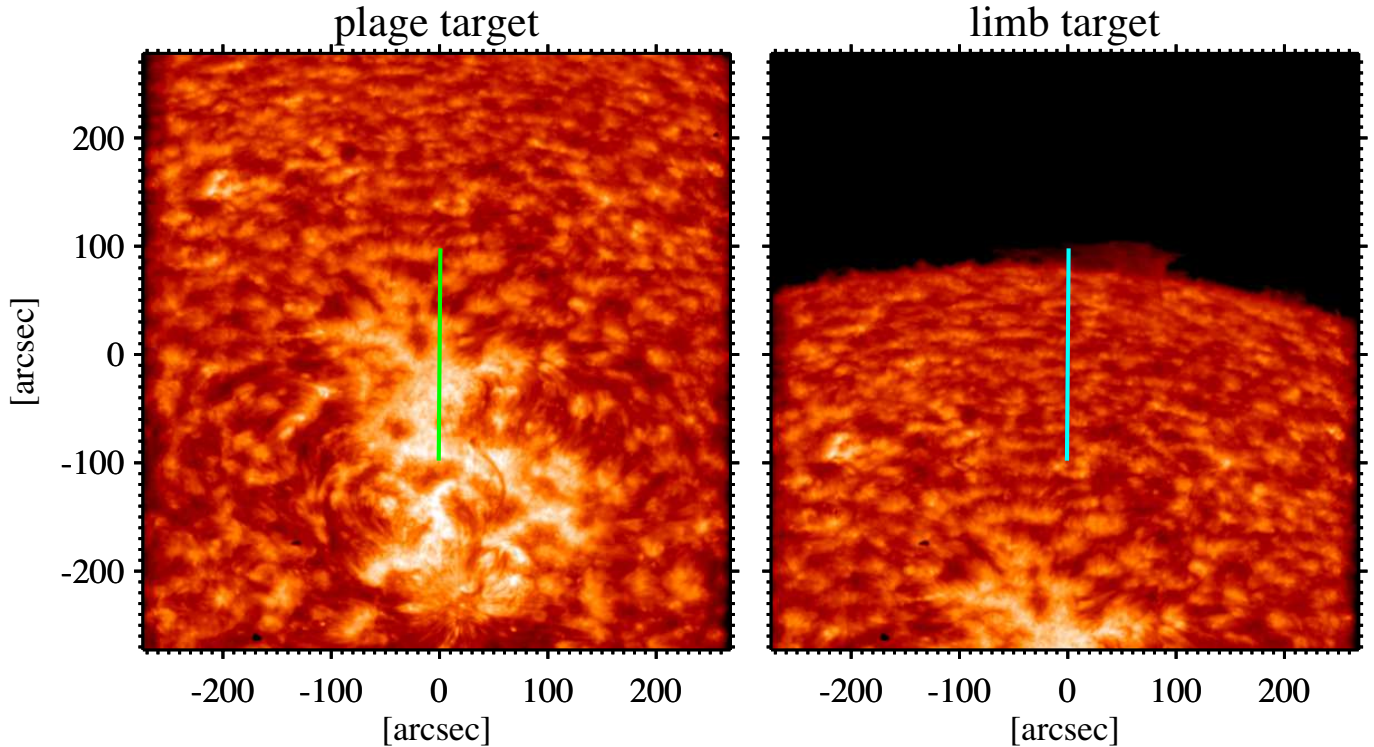
Figure 2. Broadband (FWHM=3.5 nm) intensity images taken by the CLASP2/SJ at the limb and plage targets. After correcting for pointing drift and jitter, the images were temporally averaged over 150.6 s and 137.8 s for the plage (left panel) and limb (right panel) targets, respectively. The CLASP2 spectrograph slit is indicated with solid lines following the color convention in Figure 1. The horizontal and vertical axes give the distances from the center of the spectrograph slit.

16:53:40 to 16:56:16 UT (156 s). Finally, it observed a quiet region near the limb (hereafter, limb target, see cyan box in Fig. 1) from 16:56:25 to 16:58:46 UT (141 s). The solid lines in Figure 1 showing the 30.4 nm image obtained by the Atmospheric Imaging Assembly (AIA; Lemen et al. 2012) on board the SDO, show the positions of the CLASP2 spectrograph slit, whose length is 196″ (Figure 1). The slit was roughly oriented along the radial direction.

Figure 2 shows the broadband (full width at half maximum, FWHM = 3.5 nm) Lyman-α images obtained by the CLASP2 slit-jaw monitor system (CLASP2/SJ), including the exact positions of the slit. The CLASP2/SJ uses two Lyman-α broad-band filters and it took chromospheric images with a fast cadence of 0.6 s and a plate scale of 1″03/pix (Kubo et al. 2016). In the plage target (see the left panel of Figure 2), about one third of the slit covered the relatively quiet region outside the bright region of the plage. Concerning the limb target (see the right panel of Figure 2), about $\sim$ 23″ of the slit were outside of the Lyman-α limb.

The CLASP2 spectropolarimeter has two optically symmetric channels with their respective CCD cameras, which provide simultaneous measurements in two orthogonal polarization states (Tsuzuki et al. 2020). The

two cameras recorded the modulated radiation every 0.2 s in synchronization with a polarization modulation unit (PMU: Ishikawa et al. 2015) which continuously rotates a waveplate at 3.2 s/rot (Ishikawa et al. 2013). The wavelength range covers from 279.3 nm to 280.7 nm including the Mg II h & k lines at 280.35 nm and 279.64 nm, respectively, and two Mn I lines at 280.19 nm and 279.91 nm (vacuum wavelengths). After dark and gain corrections, we demodulated the observed signals to derive the wavelength variation of the Stokes I, Q, U, and V parameters for each PMU rotation and for each channel. Subsequently, we corrected for pointing and wavelength drifts and co-registered the I, Q, U and V spectra so that the slit and wavelength directions are aligned to the CCD pixels. Then, we applied the response matrix of the CLASP2 instrument to the I, Q, U, and V spectra, which was derived in the polarization calibration investigation (Song et al. 2022). Finally, we obtain the I, Q, U, and V spectra by combining the two channels. The plate scales of the spectropolarimeter are 0.527″/pix along the slit and 0.00498 nm/pix along the dispersion direction. The spatial and spectral resolutions are $\sim$ 1.1″ and $\sim$ 0.01 nm, respectively (Song et al. 2018; Yoshida et al. 2018). The reference direction for positive (negative) Stokes Q is the paral-

lel (perpendicular) to the nearest solar limb, while the reference direction for positive (negative) Stokes U is at 45° counterclockwise (clockwise) with respect to the $Q > 0$ reference direction.

In order to maximize the polarization sensitivity, we use all the acquisitions during each pointing, resulting in temporally averaged Stokes spectra of 150.4 s and 137.6 s for the plage and limb targets, respectively. The time-averaging of the Stokes profiles smears out the influence of the dynamics (e.g., Carlin et al. 2013; del Pino Alemán et al. 2020). The present investigation concerns the interpretation of the temporally-averaged Stokes profiles. The final Stokes $I(\lambda)$ and fractional polarization spectra $Q(\lambda)/I(\lambda)$, $U(\lambda)/I(\lambda)$, and $V(\lambda)/I(\lambda)$, with λ being the wavelength (hereafter, I, Q/I, U/I, and V/I), over the whole wavelength range obtained by CLASP2 are shown in Figure 3. The distance from the disk center ranges from 546''8 to 740''9 ($0.64 \leq \mu \leq 0.82$) and from 789''2 to 984''0 ($\mu \leq 0.57$) for the plage and limb targets, respectively. μ is the cosine of the heliocentric angle, which was determined by taking the limb location at 961''5 (Rachmeler et al. 2022).

3. DATA ANALYSIS

3.1. *Wavelength-integration of the linear polarization signals*

As clearly seen in Figure 3, the Mg II k line at 279.64 nm shows significant fractional linear polarization Q/I and U/I signals, while they are zero at the very center of the Mg II h line at 280.35 nm. The Q/I pattern observed by CLASP2 in a quiet region close to the limb is consistent with the theoretical scattering polarization pattern predicted by Belluzzi & Trujillo Bueno (2012) through radiative transfer calculations with partial frequency redistribution (PRD) and quantum-mechanical interference between the upper J-levels of the Mg II k & h lines. Such calculations were carried out in the unmagnetized semi-empirical model C of Fontenla et al. (1993), representative of the quiet solar atmosphere. Recently, Rachmeler et al. (2022) compared the observed center-to-limb variation (CLV) with such radiative transfer calculations. Figures 4 and 5 show examples of the observed I, Q/I, U/I, and V/I profiles from the quiet and plage targets, respectively.

In this paper, we investigate the linear polarization signals in five ranges in the observed spectra, specifically at the far blue and red wings of the k line (violet and magenta in Figure 3, respectively), at the near blue and red wings of the k line (i.e., between the k_2 and k_1 peaks, light blue and red in Figure 3, respectively), and at the Mg II k core (i.e., a few pixels around the

k_3 line center, green in Figure 3). The Stokes signals at these wavelength ranges encode information on different layers of the solar atmosphere, roughly at the upper photosphere (far wings of the k line), at the middle chromosphere (near wings of the k line), and at the top of the chromosphere (k core), respectively (e.g., see Figure 8 of del Pino Alemán et al. 2020). In order to characterize the behavior of the scattering polarization signals, we define the following five quantities,

$$i = \sum_\lambda I(\lambda), \tag{1}$$

$$q = \frac{\sum_\lambda Q(\lambda)}{\sum_\lambda I(\lambda)}, \tag{2}$$

$$u = \frac{\sum_\lambda U(\lambda)}{\sum_\lambda I(\lambda)}, \tag{3}$$

$$LP = \frac{\sqrt{\left(\sum_\lambda Q(\lambda)\right)^2 + \left(\sum_\lambda U(\lambda)\right)^2}}{\sum_\lambda I(\lambda)}, \tag{4}$$

and

$$\chi = \frac{1}{2} \arctan\left(\frac{\sum_\lambda U(\lambda)}{\sum_\lambda Q(\lambda)}\right). \tag{5}$$

The angle of polarization χ indicates the direction of the plane of linear polarization with respect to the plane of reference (i.e., the parallel to the nearest solar limb, which is the direction for positive Stokes Q) with positive angles counterclockwise. We note that $0° \leq \chi < 45°$, $135° < \chi < 180°$ for $q > 0$ and $45° \leq \chi \leq 135°$ for $q \leq 0$ (e.g., Equations (1.8) of Landi Degl'Innocenti & Landolfi 2004). The wavelength summation in these equations is over those ranges indicated with colors in Figure 3. The exact pixels included in the integration depend on the target and slit position, as discussed in Appendix A. The spatial variations of these quantities for the five spectral ranges are shown in Appendix B.

We determine the error in these quantities from the error propagation based on the photon noise. The q, u, and LP errors are quantified with

$$\sigma_l = \frac{1}{a\sqrt{N}}, \tag{6}$$

where N is the total number of photons and $a = (1 - \cos 234°)/\pi$ the modulation coefficient (Ishikawa et al. 2014; Song et al. 2022). The noise can introduce a nonzero contribution in LP, as can be seen from Equation (4). However, such a contribution can be neglected in this analysis because the σ_l are found to be much smaller than the corresponding amplitudes of q, u, and LP (see the mean σ_l in Table 2 and the shaded areas in Figures 11 - 15).
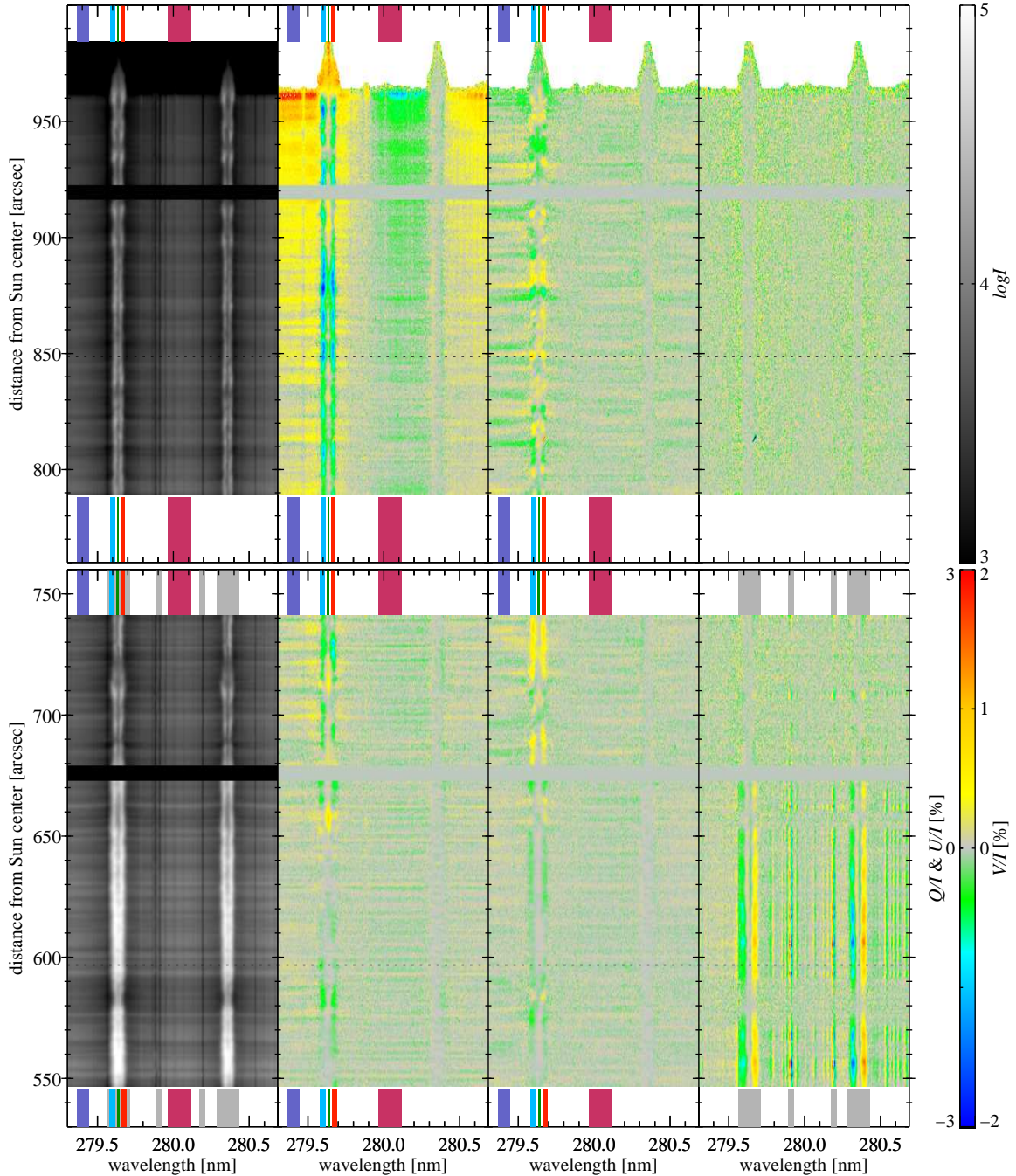
Figure 3. From left to right, temporally averaged intensity I and fractional polarization Q/I, U/I, and V/I spectra across the Mg II h & k lines obtained by CLASP2 at the limb and plage targets (upper and lower panels, respectively). The intensity I is the averaged number of electrons per exposure detected by the two channels in logarithmic scale. The data under the dust on the slit, which are shown in black (in I) and gray (in Q/I, U/I, and U/I) horizontal stripes are excluded in the analysis. The Stokes signals corresponding to each of the spectral ranges colored with violet, light blue, green, red, and magenta have been integrated for obtaining the far blue wing, the near blue wing, the core, the near red wing, and the far red wing signals explained in the text. The colors are the same as those in Figures 4 and 5. The gray areas in the I and V/I panels indicate the spectral regions of the Mg II k (279.64 nm), Mn I blue (279.91 nm), Mn I red (280.19 nm), and Mg II h (280.35 nm) lines, respectively, across which we have applied the WFA to estimate the longitudinal component of the magnetic field at different heights in the solar atmosphere.
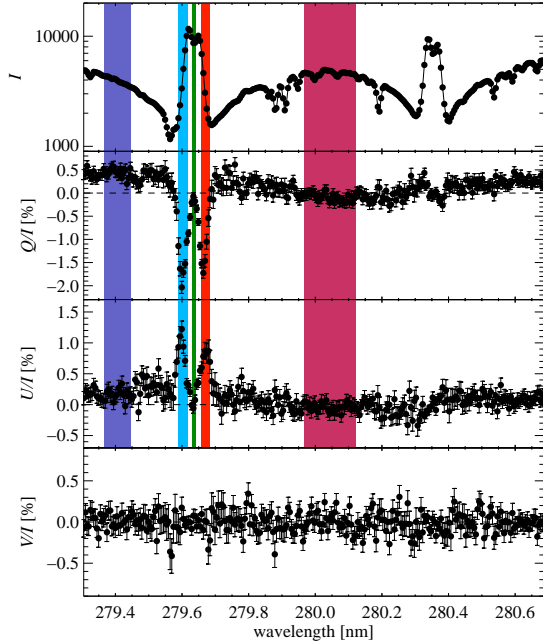
Figure 4. Stokes profiles from the limb target at the slit position indicated by the dotted line in the upper panel of Fig. 3. In the lower three panels, the error bars show $\pm 1\sigma$ errors based on the photon noise. The spectral regions colored with violet, magenta, light blue, red, and green are the same as those indicated in Fig. 3.

The error for χ is

$$\sigma_\chi = \frac{1}{2} \frac{\sigma_l}{LP}. \tag{7}$$

The large uncertainty found for certain values of χ (for example, around $680''$ in Figure 11) is due to the close-to-zero values of LP, as can be seen from the equation above.

3.2. *Longitudinal magnetic field inference*

We compare the quantities defined above with the longitudinal component of the magnetic field (B_L) inferred at several heights in the solar atmosphere. We derive B_L in the plage target from the Zeeman-induced V/I signals observed in the Mg II h & k lines and in the two Mn I lines (gray areas in Figure 3). The V/I profiles of the Mg II h (effective Landé factor $g_{\rm eff} = 1.33$) and k ($g_{\rm eff} = 1.167$) lines consist of two external lobes and two inner lobes of smaller amplitude (see also the bottom panel of Figure 5). These external and inner lobes of V/I encode information on the magnetic field at the middle and top layers of the chromosphere, respectively (del Pino Alemán et al. 2020). The V/I profiles of the two Mn I lines at 279.91 nm ($g_{\rm eff} = 1.94$) and 280.19 nm ($g_{\rm eff} = 1.7$) have only two lobes, which provide information at the bottom of the chromosphere (del Pino Alemán et al. 2022).
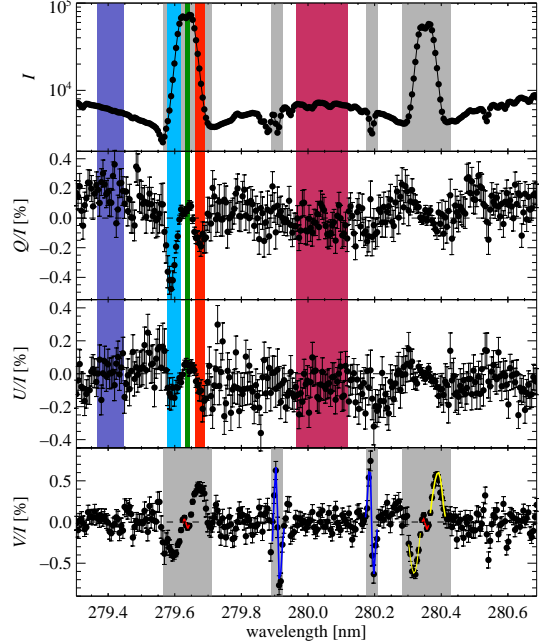
Figure 5. Stokes profiles from the plage target at the slit position indicated by the dotted line in the lower panel of Fig. 3. In the lower three panels, the error bars show $\pm 1\sigma$ errors based on the photon noise. The spectral regions colored with violet, magenta, light blue, red, green, and gray are the same as those indicated in Fig. 3. The red, yellow, and blue curves in the V/I bottom panel show the fits that result from the application of the WFA to the inner lobes of the Mg II h & k lines, to the external lobes of the Mg II h line, and to the Mn I lines, respectively.

We infer B_L by applying the WFA exactly as we did in Ishikawa et al. (2021). PRD has an impact on the amplitudes of the external lobes of the h & k lines and thus the WFA tends to underestimate B_L (Alsina Ballester et al. 2016; del Pino Alemán et al. 2016). Such an underestimation is more significant in the k line. Moreover, the blue wing of the k line is blended with the Mn I line. Therefore, we apply the WFA only to the external lobes of the h line to infer the B_L at the middle chromosphere. The resulting spatial variations of B_L along the slit of the spectrograph are shown in Appendix B (bottom panels of Figures 11−15). The 1σ error of B_L (σ_B) is also obtained based on the uncertainty of V/I due to the photon noise. Note that no significant V/I signals are detected at the quiet limb target (upper panel of Figure 3) and thus we only infer B_L at the plage target.

4. RESULTS

4.1. *Sign change of u*

The geometrical complexity of the upper solar chromosphere has a crucial impact on the scattering polarization of strong resonance lines (Trujillo Bueno et al.
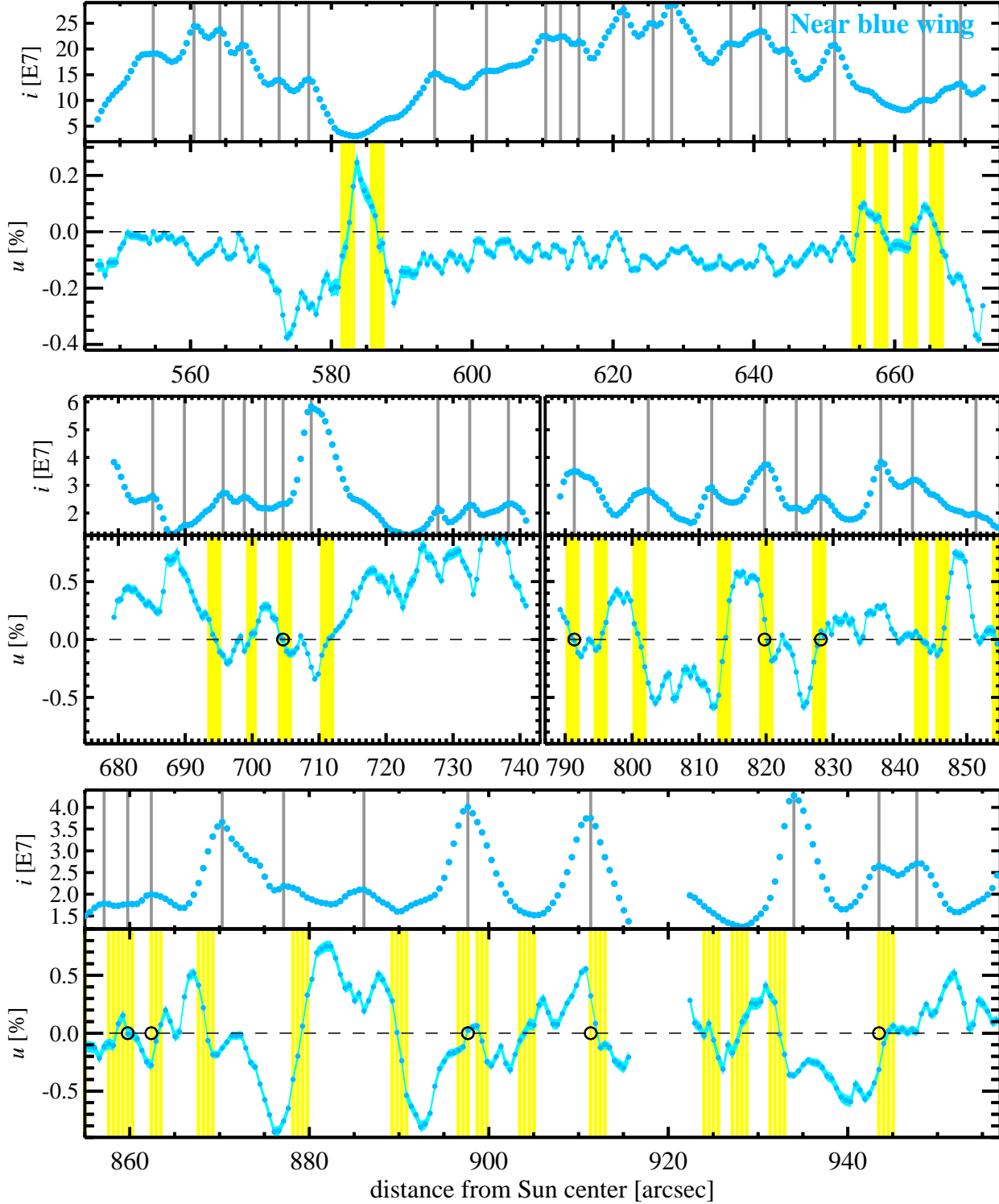
Figure 6. Spatial variation of i and u at the near blue wing of the Mg II k line (see the light blue spectral range in Fig. 3), calculated with Equations (1) and (3), respectively. The shaded area in cyan in the panels for u show $\pm\sigma_l$ errors. The top panel corresponds to the bright region of the plage, while the middle and bottom panels correspond to the quiet region. The locations where the intensity presents a local maximum are indicated by gray vertical lines, while the ones where u changes the sign are shown by yellow vertical stripes. The black circles show the positions where these local maxima are co-located with u zero-crossing locations.
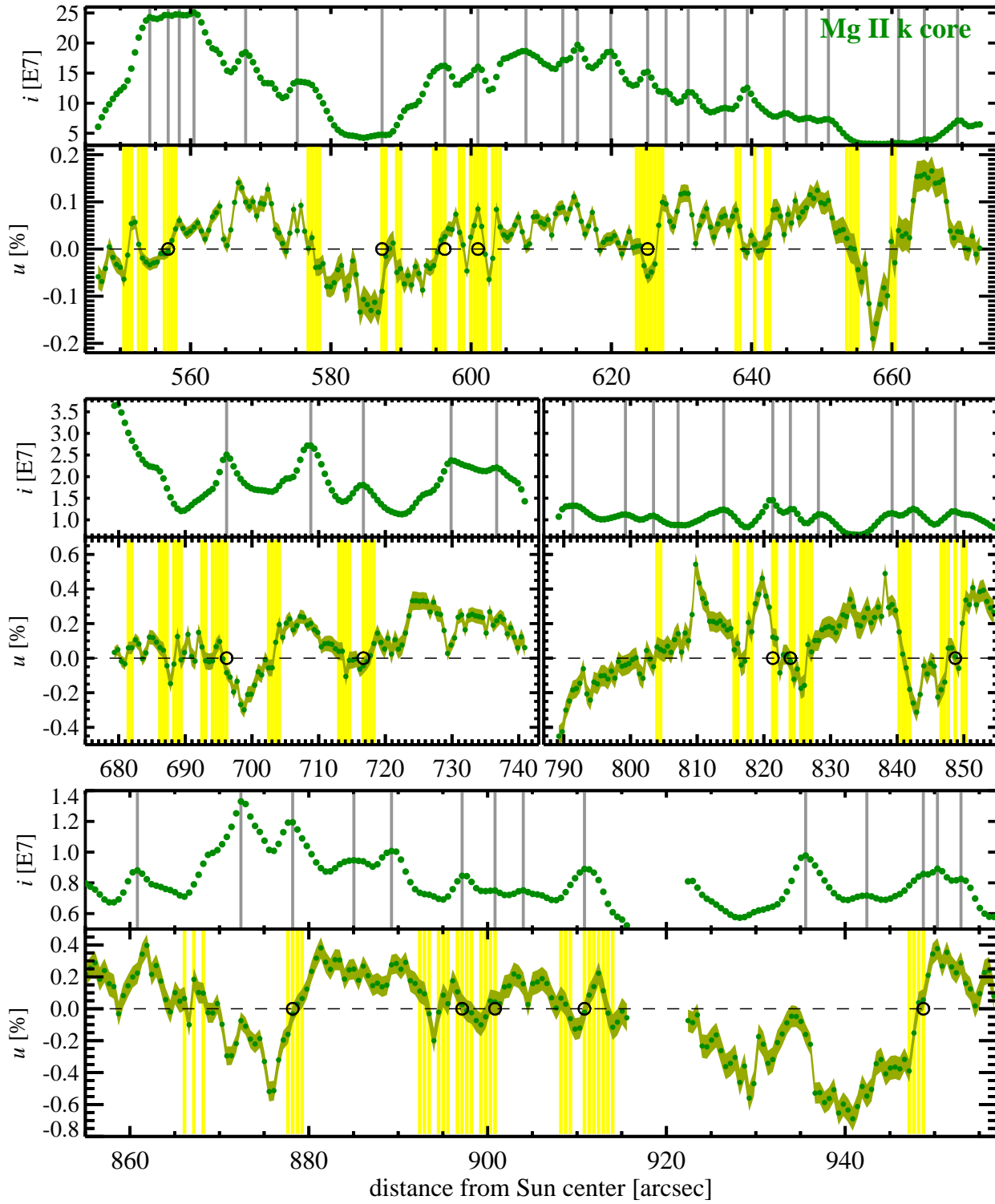
Figure 7. Same as Fig. 6, but for the core of the Mg II *k* line (see green spectral range in Fig. 3).

2018). This impact is due to the lack of axial symmetry of the incident radiation field (i.e., the radiation that illuminates each point within the medium), caused by the horizontal inhomogeneities of the solar atmospheric plasma and/or by the gradients of the macroscopic velocities. In their analyses of the CLASP1 observations of the scattering polarization in the hydrogen Lyman-α and in the resonance line of Si III, Ishikawa et al. (2017) searched for signatures indicating a lack of such axial symmetry. They noted that in the wings of the Lyman-α line, where the Hanle effect does not operate, the U/I signal tends to change its sign around the spatial locations where the Lyman-α intensity at the same wavelength shows a local maximum value. As schematically shown in their Figure 7 (see also Štepán & Trujillo Bueno 2012), the correlation between the sign change in the U/I wing signal and the local maxima in intensity is consistent with the scattering signals due to the lack of axial symmetry. Here, we investigate whether a similar behavior is present across the Mg II h & k lines.

Figures 6 and 7 show the spatial variation of i (Equation (1)) and u (Equation (3)) at the near blue wing and the core of the k line (see also Figures 16, 17, and 18 in Appendix C for the far blue wing, the far red wing, and the near red wing of the k line, respectively). We mark the pixels $x_{\max}$ where the i signals show a local maximum (gray vertical line) and then examine whether the u signal changes its sign (i.e., crosses zero) around such spatial locations. If the signs of u at two neighboring pixels around $x_{\max}$ are opposite (i.e., $u_{x_{\max}-1} \cdot u_{x_{\max}+1} < 0$ or $u_{x_{\max}-2} \cdot u_{x_{\max}+2} < 0$) we classify this pixel as a u zero-crossing point (black circle in the figure). However, if the u signal at any of such neighboring pixels turns out to be smaller than the noise level (e.g., $|u_{x_{\max}-1}| < \sigma_{x_{\max}-1}$) and its sign is opposite to that corresponding to the outer neighboring pixel (e.g., $u_{x_{\max}-1} \cdot u_{x_{\max}-2} < 0$), we do not count it as a zero-crossing point.

Table 1 summarizes the number of identified i local maxima and u zero-crossing points. The region at a distance from the Sun center of less than $673''$ (i.e., the area below the dust in the bottom panel of Figure 3) is what we call plage region (top panels in Figures 6 and 7, and in Figures 16, 17, and 18 in Appendix C), since at most of the slit positions we find a sizable longitudinal component of the magnetic field. The remaining regions (i.e., the area above the dust in the bottom panel of Figure 3 and the region in the top panel of Figure 3) are what we call quiet region. In the quiet region, we find that at the considered wavelength ranges the u signal changes sign in more than roughly 30% of the locations

where i shows a local maximum. In the plage region, some of the locations with local maxima are cospatial with a change in the sign of u. However, the fraction of u zero-crossing points associated with local maxima in i is lower than in the quiet Sun region, except in the case of the Mg II k far red wing (see also Figure 17).

We investigate whether the number of local i maxima which are co-located with a change in the sign of u (hereafter, the number) can be explained by random chance (see Appendix D). In the quiet region, the number is larger than the mean that would be expected in the random chance scenario by at least 1σ at all considered wavelength ranges and at the 2σ level in the core and red wing ranges. On the other hand, in the plage region, for the k core, near red wing, and far blue wing, the spatial coexistence of the local intensity maxima and u zero-crossing is consistent with random chance. In the near blue wing, the number is smaller than the mean expected due to random chance by 1σ. As in the quiet region, at the far red wing, the number exceeds the mean in the random chance case by 2σ.
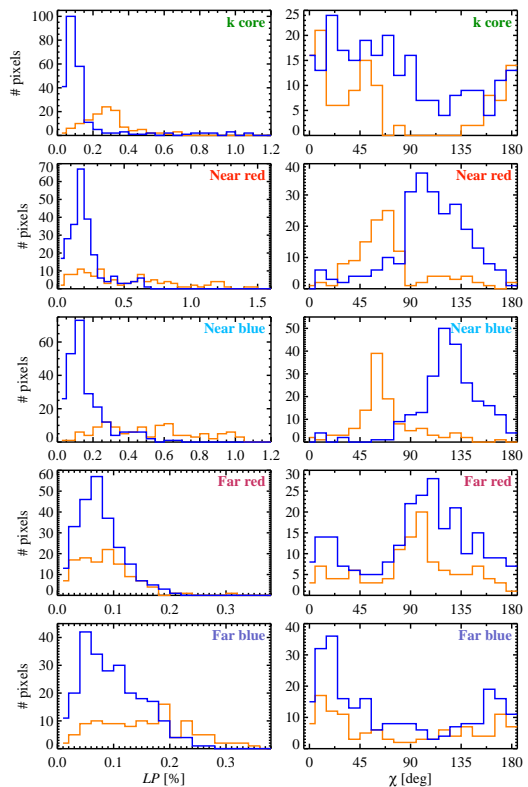
Figure 8. Histograms of LP (left column) and χ (right column) for the quiet (in orange, at the distance from the Sun center of $679'' - 741''$) and the plage (in blue, at $547'' - 673''$) regions and the following wavelength ranges of the Mg II k line (from top to bottom): core, near red and blue wings, and far red and blue wings.

	Plage		Quiet Sun	
	#i max.	#u zero-cross	#i max.	#u zero-cross
Mg II k core (green)	24	5 (21%)	30	10 (33%)
Mg II k near blue wing (light blue)	20	0 (0%)	31	9 (29%)
Mg II k near red wing (red)	26	4 (15%)	30	10 (33%)
Mg II k far blue wing (violet)	31	9 (29%)	62	23 (37%)
Mg II k far red wing (magenta)	33	21 (64%)	59	34 (58%)

Table 1. Number of i maxima and u zero-crossing points for the plage and quiet regions at the selected spectral ranges, namely at the core (green in Fig. 3), the near blue and red wings (light blue and red in Fig. 3, respectively) and at the far blue and red wings (violet and magenta in Fig. 3, respectively) of the Mg II k line. The plage region pixels are those at distances from the disk center of $543'' - 673''$ while the quiet region pixels are those with $679'' - 984''$. The values within parenthesis give the fraction of u zero-crossings with respect to the number of i maxima.
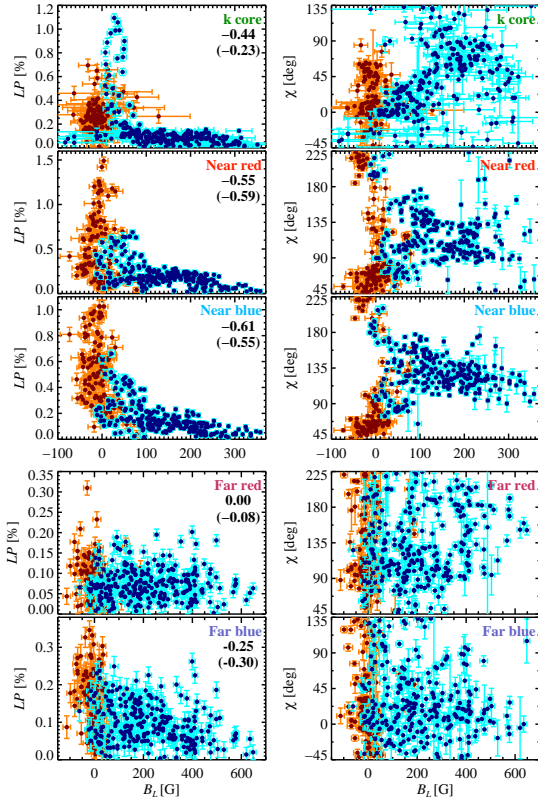
Figure 9. Scatter plots of LP vs. B_L (left column) and of χ vs. B_L (right column) for each of the selected wavelength ranges. The dark blue points with cyan error bars ($\pm\sigma_B$, $\pm\sigma_l$, or $\pm\sigma_\chi$) correspond to the plage region at the distance from the Sun center of $547'' - 673''$, whereas the brown points with orange error bars correspond to the quiet region at $679'' - 741''$. The numbers shown within each panel in left column are the correlation coefficients between LP and B_L for the plage region (dark blue points). The values in parenthesis are the coefficients for the plage pixels with $B_L > 100$ G.

4.2. Dependence of LP and χ on B_L

In this section, we study how the degree of linear polarization LP (Equation (4)) and the linear polarization angle χ (Equation (5)) vary with B_L, with the aim of investigating the impact of magnetic fields on the scattering polarization across the Mg II h and k lines. In the quiet Sun target close to the limb, the lack of V/I signals does not allow for the inference of the longitudinal component of the magnetic field. Therefore, we limit our investigation to the plage target pixels and classify them into two groups depending on the distance from the Sun center: $574'' - 673''$ as the plage region (below the dust in the lower panel of Fig. 3) and $679'' - 741''$ as the quiet region (above the dust in the lower panel of Fig. 3).

4.2.1. LP distribution

The left column of Figure 8 shows the LP histograms of the plage (blue) and the quiet (orange) regions for the previously indicated five wavelength ranges. In most of the wavelength ranges, the quiet region shows a wider distribution of LP values (for example, from 0% to 1.5% at the near red wing) than in the plage region. Moreover, the quiet region histograms for the near red and blue wings and for the far blue wing do not show any significant peak. In contrast, in the plage region, each of the LP histograms shows a clear peak at relatively low LP values. Especially at the core, near red and blue wings of the Mg II k line, the LP distributions are clearly different between the quiet and plage regions, clearly indicating that the weakly magnetized region tends to have larger LP signals.

The left column of Figure 9, which shows the scatter plots of LP vs. B_L (Section 3.2) for the quiet (brown points with orange error bars) and the plage (dark blue with cyan error bars) regions, for the five selected spectral ranges, allows to investigate the behavior of LP with B_L. We compare LP with B_L at the approximate height of formation of each spectral range indicated with a color in Figure 3, namely, LP at the core of the Mg II k

line vs. B_L at the top of the chromosphere (estimated via the inner lobes of V/I of the Mg II h & k), LP at the near blue and red wings of the Mg II k vs. B_L at the middle chromosphere (estimated via the external lobes of V/I of the Mg II k), and LP at the far blue and red wings vs. B_L at the bottom chromosphere (estimated via the V/I signals of the Mn I lines). It can be observed that at the Mg II k core, the pixels with the largest LP belong to the plage region although their field strength is relatively weak ($B_L < 50$ G). The high LP region extends for $10''$, showing its peak at $657''$(see fourth panel from the top in Figure 11). Such an enhancement of LP comes from the strong Q/I signal and is visible only in the k core (see Q/I spectra in Figure 3). In this region, the Mg II intensity spectra show clear self-absorption at the core. We attribute the large-amplitude Q/I signals found at such spatial points to scattering polarization and we note that, if they originated from the Zeeman effect due to the transverse component of the magnetic field, similar linear polarization signals should also be detected in the h line.

There seems to be a negative correlation between LP and B_L (i.e., LP is the smaller for stronger B_L) at the core and the near red and blue wings of k line as shown by the linear Pearson correlation coefficients given inside each panel. In the near blue and red wings, the coefficients remain similar when considering only the pixels where $B_L > 100$ G, but it becomes smaller in the core (see the values in the parenthesis). On the other hand, at the far red and blue wings of the Mg II k line (bottom two panels of Figure 9), LP varies over a wide range of values regardless of the B_L value, with no significant differences between the quiet and plage regions: there is no evidence of correlation between LP and B_L in neither the plage or quiet regions. Indeed, the correlation coefficients between LP and B_L are 0.0 at the far red wing and -0.25 at the far blue wing, which are smaller than at the core and near wings of the k line and do not change very much for the pixels with $B_L > 100$ G.

4.2.2. χ distribution

The right column of Figure 8 shows the χ histograms for the five selected spectral ranges. Note that there is a 180° ambiguity in χ ($\chi = \chi + 180° \times m$ with $m = 0, \pm 1, \pm 2, \ldots$). Radiative transfer calculations in an unmagnetized semi-empirical 1D model atmosphere predict $U = 0$ and $Q > 0$ (i.e., $\chi = 0°$) at the core, $Q < 0$ (i.e., $\chi = 90°$) at the near blue and red wings, $Q > 0$ (i.e., $\chi = 0°$) at the far blue wing, and $Q < 0$ (i.e., $\chi = 90°$) at the far red wing of the k line (Belluzzi & Trujillo Bueno 2012; del Pino Alemán et al. 2016; Alsina Ballester et al. 2016). The quiet Sun his-

tograms shown in orange are roughly consistent with this prediction. For example, the histogram of the k core shows high frequency around 0° or 180°. The peaks of the quiet Sun histograms for the near blue and red wings deviate from 90° by $20° - 30°$.

At the far red and blue wings (bottom two panels), the χ histograms in the plage region are similar to those in the quiet region. In the plage region there also seems to be a preference in χ for $\sim 90°$ at the far red wing and for $\sim 0°$ at the far blue wing, respectively, as in the quiet region. However, at the near red and blue wings and the core (upper three panels), the quiet and plage region histograms are different. At the near red and blue wings, most of the quiet region pixels have $0° \leq \chi \leq 90°$, while most of the plage region pixels have $90° \leq \chi \leq 180°$. At the core of the k line, the plage region pixels show a more uniform distribution, with a non-negligible number of pixels with $67.5° \leq \chi \leq 135°$, while this behavior is not found in the quiet Sun pixels.

The right column of Figure 9 shows the scatter plots of χ vs. B_L. The assignment of B_L for the comparison with each selected spectral range is the same as in the left column of Figure 9. The linear polarization angle χ has a 180° ambiguity and we choose the plot range so that the majority of the plage pixels can smoothly cluster in each panel (i.e., $-45° \leq \chi \leq 135°$ for the core and the far blue wing of the k line, and $45° \leq \chi \leq 225°$ for the near red, near blue, and far red wings). In the core of the k line, the quiet region distribution (brown points) lies around 0°, although the variation is relative large (i.e., roughly $\pm 45°$). The plage region pixels, where $|B_L| < 100$ G, are also clustered around 0°. However, in the pixels where B_L is larger, they scatter over a wide range of χ with some preference for $45° < \chi < 90°$ at $150 < B_L < 250$ G.

At the near blue and red wings, most of the quiet region pixels are clustered at $45° \leq \chi \leq 90°$ and $180° \leq \chi \leq 225°$, which correspond to $0° \leq \chi \leq 90°$ in Figure 8. However, the behavior of χ in the plage is very different. The plage pixels with $B_L \lesssim 50$ G show $\sim 90°$ and $\sim 180°$, which are at the outer edges of the clusters of the quiet region pixels ($45° \leq \chi \leq 90°$ and $180° \leq \chi \leq 225°$). Moreover, most of the plage pixels with stronger field of $B_L > 100$ G tend to concentrate at $90° \leq \chi \leq 135°$. Finally, at the far blue and red wings, we cannot find any clear characteristic behavior with B_L in either the quiet or plage regions.

In summary, at the core and the near wings of the Mg II k line, the LP and χ distributions are significantly different between quiet and plage regions, and these properties seem to be dependent on B_L. On the other hand, at the far wings of the Mg II k line, we do

not find any difference nor dependence on B_L as clear as at the core and the near wings.

5. DISCUSSION

CLASP2 succeeded in obtaining the first spatially and spectrally resolved measurements of the linear and circular polarization signals across the solar Mg II h & k lines. The Zeeman-induced circular polarization signals have allowed us to determine the longitudinal component (B_L) of the magnetic field at three different heights of the solar chromosphere (top, middle, and bottom[3]) via the application of the WFA to the Mg II h & k and the Mn I lines (Ishikawa et al. 2021). Recently, by comparing the CLASP2 observations with the theoretical calculations of Belluzzi & Trujillo Bueno (2012), it has been confirmed that PRD and J-state interference play a crucial role in producing the scattering polarization signals across the Mg II h & k lines (Rachmeler et al. 2022). The linear polarization signals of these resonance lines encode information on the magnetic fields of the solar chromosphere through the Hanle and MO effects. Thanks to the unique data provided by CLASP2, in this paper we have investigated the linear polarization signals observed at different spectral ranges across the Mg II h & k lines, comparing them with our estimation of B_L at their approximate heights of formation in the solar chromosphere.

Our aim has been to clarify the impact of the magnetic field on the linear polarization signals across these ultraviolet lines. Depending on the selected wavelength range, the effects can be different, because of the different heights of formation and the different mechanisms that introduce magnetic sensitivity in the core and wings of the lines. Thus, we have analyzed separately the linear polarization signals at the k-line core, at the near blue and red wings, and at the far blue and red wings of the Mg II k line. We point out that an analysis of the amplitude of the Q/I profile alone is not sufficient to judge on the possible operation of the Hanle and the MO effects. Such amplitude heavily depends on the anisotropy of the radiation field, which in turn primarily depends on the temperature stratification of the atmosphere in the observed region. The latter may strongly vary moving from a quiet region to a plage. Indeed, while the emergent intensity in the 1D semi-empirical model P of Fontenla et al. (1993), which is representative of a plage region, is significantly larger than in

their quiet Sun model C due to its enhanced temperature below the transition region, the P model shows less fractional linear polarization (Trujillo Bueno et al. 2017; del Pino Alemán et al. 2020) because of the smoother temperature gradient (Ishikawa et al. 2018). Thus, we have investigated also the U/I and the behavior of the linear polarization angle χ.

First, we focus on the spatial variation of the U/I signals, which are induced by the presence of the magnetic fields (via the Hanle and MO effects) and by the lack of axial symmetry of the radiation field. In the quiet region, where B_L is relatively low, we find that in about 30% of the bright structures (local intensity maxima) the U/I signals change their sign (i.e., U/I crosses zero), both at the core of the k line (where the Hanle effect operates) and at the wings (where the MO effects operate). The numbers of spatial coincidences between the local intensity maxima and the U/I zero-crossings are larger than those expected from random coincidence, at $1-2\sigma$ levels depending on the considered wavelength range. However, in the plage region, where B_L is substantial, reaching up to 350/650 G at the top/bottom chromosphere, the fraction of bright structures where the U/I signals change their sign seem to be smaller, except in the far red wing of the Mg II k line. Indeed, in the plage region, the number of spatial coincidences is consistent with the number that would be expected from the random chance case (core, near red wing, far blue wing) or it is smaller at 1σ significance (near blue wing). In the plage region, the number of spatial coincidences in the far red wing exceeds the expected random chance mean at 2σ significance.

Next, we have investigated whether the behavior of the total linear polarization (LP) and the linear polarization angle (χ) is different between the quiet and plage regions and whether it varies with B_L. Interestingly, we find that at all the selected wavelength ranges, LP is significantly suppressed in the plage region. Moreover, especially at the core and the near wings of the k line, we find anticorrelation between LP and B_L. At the core and the near wings of the Mg II k line, the χ distribution is also different in the quiet and plage regions especially in the pixels where $B_L > 50$ G. On the other hand, at the far wings of the k line, the χ distributions in the quiet and plage regions are similar and we do not find any dependence of χ on B_L.

The smaller fraction of U/I zero-crossing points in the plage region may be interpreted as due mainly to the influence of the magnetic fields through the Hanle and MO effects, dominating over that caused by the lack of axial symmetry. The smaller LP and the change of χ can be interpreted as manifestations of the depolarization and

---

[3] The bottom chromosphere is the region just above the temperature minimum in standard semi-empirical models. The top chromosphere is just below the height at which the temperature begins to rise dramatically. The middle chromosphere is the intermediate zone between them.

rotation of the plane of linear polarization caused by the Hanle and MO effects. These three observational signatures are found in the plage region at the core and the near wings of the Mg II k line, and we consider them as evidence for the operation of the Hanle and MO effects. Note that any change of the linear polarization signals found in this analysis is not due to the transverse Zeeman effect. If this was the case, we should see corresponding signals in the Mg II h line, which is more sensitive to the Zeeman effect than the k line because it has a larger effective Landé factor.

In the χ vs. B_L scatter plots of Figure 9, the pixels with $B_L > 100$ G tend to concentrate at $45° < \chi < 90°$ in the core of the k-line and at $90° < \chi < 135°$ in the near wings of the k line. For field strengths $B > 100$ G, the Hanle effect at the k-line core is in its saturation regime and the linear polarization signal is sensitive only to the orientation of the magnetic field (see the two top panels of Figure 9 of del Pino Alemán et al. 2020). The MO effects are still sensitive to the magnetic field strength and orientation for such relatively strong fields, although the sensitivity to the strength is not as high as for weaker fields. Thus, these concentrations around $B_L > 100$ G in the χ vs. B_L scatter plots may be compatible with the typical strong magnetic field configuration of plage regions. In the core of the k line, for the plage pixels with $B_L > 100$ G, the anti-correlation between LP and B_L is less significant, and LP seems to be completely suppressed. This property would be consistent with the Hanle saturation regime.

At the far wings, which originate in the upper photosphere, we find only one observational signature suggestive of the operation of the MO effects (i.e., small LP in the plage region) and evidence for the operation of the MO effects as clear as that found for the near wings could not be obtained. In general, the impact of MO effects is stronger in the near wings than in the far wings where the relative impact of the continuum is stronger (e.g., Section 5 of Alsina Ballester et al. 2018). Moreover, in the Mg II h & k lines, as clearly shown in the response function to the magnetic field in Figure 8 of del Pino Alemán et al. (2020), the stronger response

occurs higher in the atmosphere (i.e., near wings of the k line) than lower in the atmosphere (i.e., far wings of the k line) via the MO effects.

In this paper, we have provided purely observational evidence on the operation of the Hanle and MO effects in the scattering polarization of the Mg II h & k lines. The theoretical modeling of the unprecedented spectropolarimetric data provided by CLASP2 will be the subject of future papers. To that end, new plasma diagnostic tools are being developed, such as a new Stokes inversion code (Li et al. 2022) and a spectral synthesis code that takes into account the effects of horizontal radiative transfer. Such ongoing developments are important steps to infer the full vector magnetic field in the plage chromosphere through the Zeeman, Hanle, and MO effects in the near-UV region of the Mg II resonance lines.

APPENDIX

A. WAVELENGTH RANGES FOR INTEGRATION

We use temporally and spatially averaged Stokes spectra to select the wavelength ranges where the core and near wing signals of the Mg II k line are integrated (Equations $(1) - (5)$), and we distinguish between the plage region (at the distance from the Sun center of $547'' - 673''$, below the dust of the plage target shown in the bottom panel of

position	plage $547'' - 673''$	quiet region near plage $679'' - 741''$	near-limb quiet region $789'' - 984''$
Mg II k core	$-0.005 \leq \lambda_k \leq 0.005$ nm	$-0.005 \leq \lambda_k \leq 0.005$ nm	$-0.0025 \leq \lambda_k \leq 0.0025$ nm
	(3 pixels)	(3 pixels)	(2 pixels)
	$\overline{\sigma_l} = 0.020\%$	$\overline{\sigma_l} = 0.046\%$	$\overline{\sigma_l} = 0.067\%$
Near blue wing	$-0.060 \leq \lambda_k \leq -0.025$ nm	$-0.050 \leq \lambda_k \leq -0.025$ nm	$-0.047 \leq \lambda_k \leq -0.022$ nm
	(8 pixels)	(6 pixels)	(6 pixels)
	$\overline{\sigma_l} = 0.017\%$	$\overline{\sigma_l} = 0.042\%$	$\overline{\sigma_l} = 0.042\%$
Near red wing	$0.025 \leq \lambda_k \leq 0.05$ nm	$0.025 \leq \lambda_k \leq 0.045$ nm	$0.022 \leq \lambda_k \leq 0.042$ nm
	(6 pixels)	(5 pixels)	(5 pixels)
	$\overline{\sigma_l} = 0.022\%$	$\overline{\sigma_l} = 0.040\%$	$\overline{\sigma_l} = 0.049\%$
far blue wing	$279.37 \leq \lambda \leq 279.44$ nm (16 pixels)		
	$\overline{\sigma_l} = 0.024\%$	$\overline{\sigma_l} = 0.027\%$	$\overline{\sigma_l} = 0.032\%$
far red wing	$279.97 \leq \lambda \leq 280.12$ nm (31 pixels)		
	$\overline{\sigma_l} = 0.016\%$	$\overline{\sigma_l} = 0.018\%$	$\overline{\sigma_l} = 0.021\%$

Table 2. Summary of the selected spectral ranges for the core, the near red and blue wings, and the far blue and red wings of the Mg II k line. The position is the distance from the Sun center (see Fig 3). λ_k is the wavelength with respect to the line center of the averaged Mg II k intensity profile in each region (i.e., plage, quiet Sun near the plage, and quiet Sun near the limb, see Fig. 10), while λ is the absolute wavelength. The number of selected wavelength pixels is shown in parenthesis for each spectral interval. The mean value of the uncertainty of q, u, and LP (Equation (6)) is derived at each wavelength range and at each position ($\overline{\sigma_l}$). Note that $\overline{\sigma_l}$ for the near-limb quiet region takes into account the pixels at less than $950''$, i.e., removing the off-limb pixels.

Figure 3), the quiet region near the plage ($679'' - 741''$, above the dust of the plage target), and the quiet region of the limb target ($789'' - 984''$, upper panel of Figure 3, except for the dust). The resulting averaged spectra are shown in Figure 10. Note that after deriving the spatially and temporally averaged I, Q, and U, we take the ratio to derive the Q/I and U/I profiles.

Two or three pixels were chosen for studying the signals at the core of the Mg II k line (the area highlighted in green). The light blue and red colored bands refer to the near blue and near red wings pixels of the Mg II k line, which are selected to fully cover the Q/I and U/I lobes in the wings. The selected wavelength ranges for each region are given in Table 2.

B. SCATTERING POLARIZATION SIGNALS AND B_L

The variation of the quantities characterizing the scattering polarization (i.e., i, q, u, LP, and χ defined in Equations (1) - (5)) with the distance from the Sun center is shown in Figures $11 - 15$. The bottom panels of the figures show the longitudinal components of the magnetic field (B_L) at each slit position, inferred by applying the WFA to the V/I profiles (see Section 3.2).

C. SPATIAL VARIATION OF i AND u

Figures $16 - 18$ represent the spatial variations of i (Equation (1)) and u (Equation (3)) at the far blue and red wings and at the near red wing of the k line, which are not shown in the main text.

D. HYPOTHESIS TESTING FOR U ZERO-CROSSING

In this section, we investigate whether the spatial coincidence of local intensity maxima and u zero-crossings is due to random chance. For this purpose, we test the hypothesis that the u zero-crossing location is randomly distributed and that local intensity maximum position coincides with u zero-crossing location by chance (i.e., the null hypothesis).

Assuming that the probability that a given pixel corresponds to a u zero-crossing location is p, the probability that exactly k locations with local intensity maxima are co-spatial with zero-crossing locations out of n locations follows the binomial distribution. The mean and standard deviation of the number of coincidences are $\mu = np$ and $\sigma = \sqrt{np(1-p)}$. Defining the number of pixels which are identified to be u zero-crossing locations as s (pixels
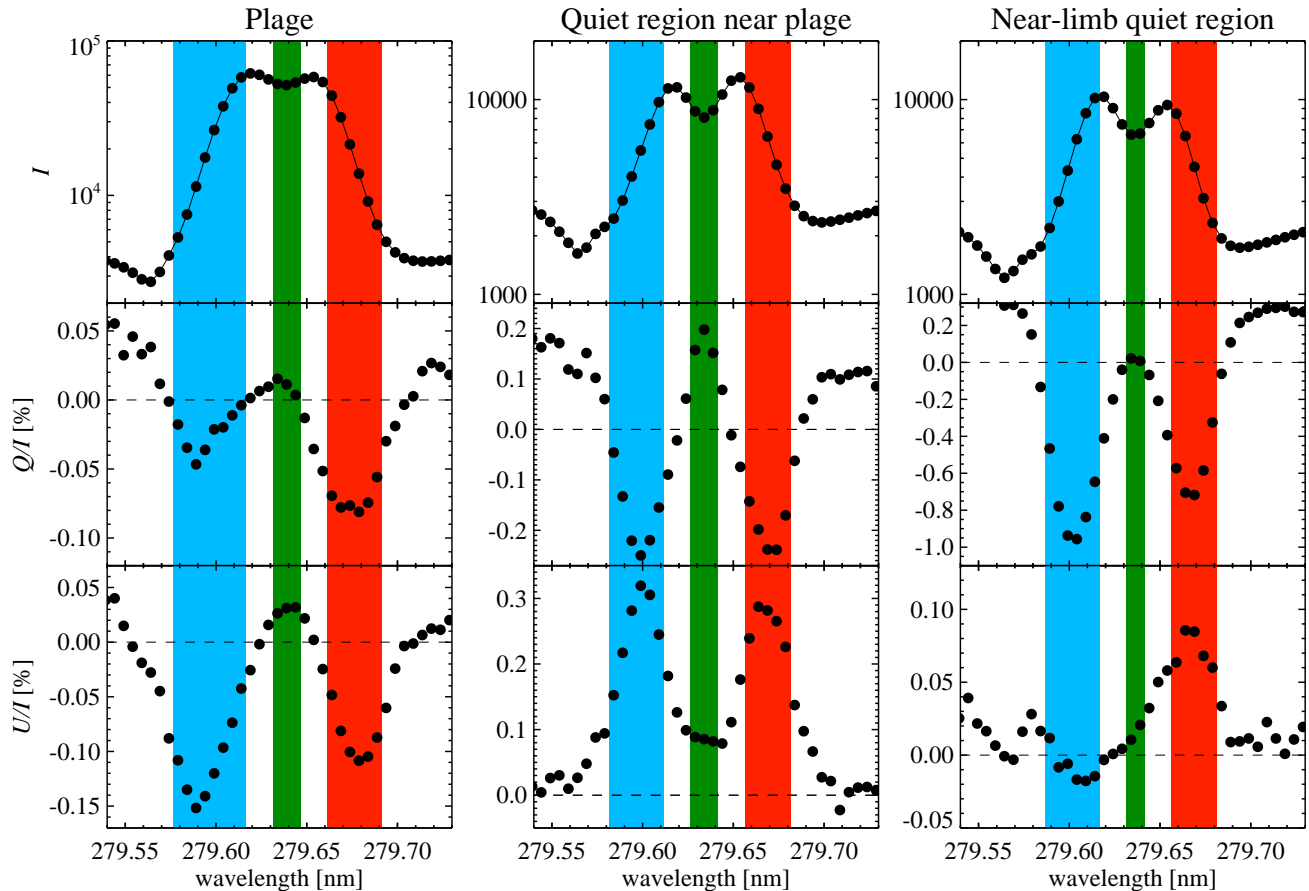
Figure 10. From top to bottom: Spatially and temporally averaged Stokes I, Q/I, and U/I profiles for the plage (left), the quiet region near the plage (middle), and the near-limb quiet region (right). Photon noise is negligibly small as a result of the spatial averaging over relatively large sections of the slit and thus is not shown here. The light blue, red, and green colored bands show the wavelength ranges for the near blue and red wings and the core of the k line, respectively, and the same as those indicated in Fig. 3.

indicated with yellow vertical stripes in Figures 6, 7, 16−18) and the total numbers of pixels in the plage and quiet regions as S, the probability p is given by s/S.

These statistical values, for quiet and plage regions, are tabulated in Tables 3 and 4, respectively. In the quiet region, the identified number of local intensity maxima that are co-spatial with u zero-crossing locations exceeds the number from random chance at the 1σ level at all considered wavelength ranges, and at 2σ level in the core and red wing ranges. On the other hand, in the plage region, the number of local intensity maxima that is co-spatial with u zero-crossing locations is consistent with random chance within the 1σ range for the core, near red and far blue wings of the k line. For the near blue wing, the number of spatial coincidences is 1σ below the mean for the random case and, for the far red wing, the number is 2σ larger than the mean (as in the quiet region). Further statistics are needed to reject the null hypothesis confidently at 2σ level: $n \geq 38$ for the near blue wing and $n \geq 192$ for the far blue wing in the quiet region, and $n \geq 51$ for the near blue wing in the plage region.

REFERENCES

Alsina Ballester, E., Belluzzi, L., & Trujillo Bueno, J. 2016, ApJL, 831, L15, doi: 10.3847/2041-8205/831/2/L15

—. 2018, ApJ, 854, 150, doi: 10.3847/1538-4357/aa978a

—. 2019, ApJ, 880, 85, doi: 10.3847/1538-4357/ab1e41

Bellot Rubio, L., & Orozco Suárez, D. 2019, Living Reviews in Solar Physics, 16, 1, doi: 10.1007/s41116-018-0017-1

Belluzzi, L., & Trujillo Bueno, J. 2012, The Astrophysical Journal Letters, 750, L11
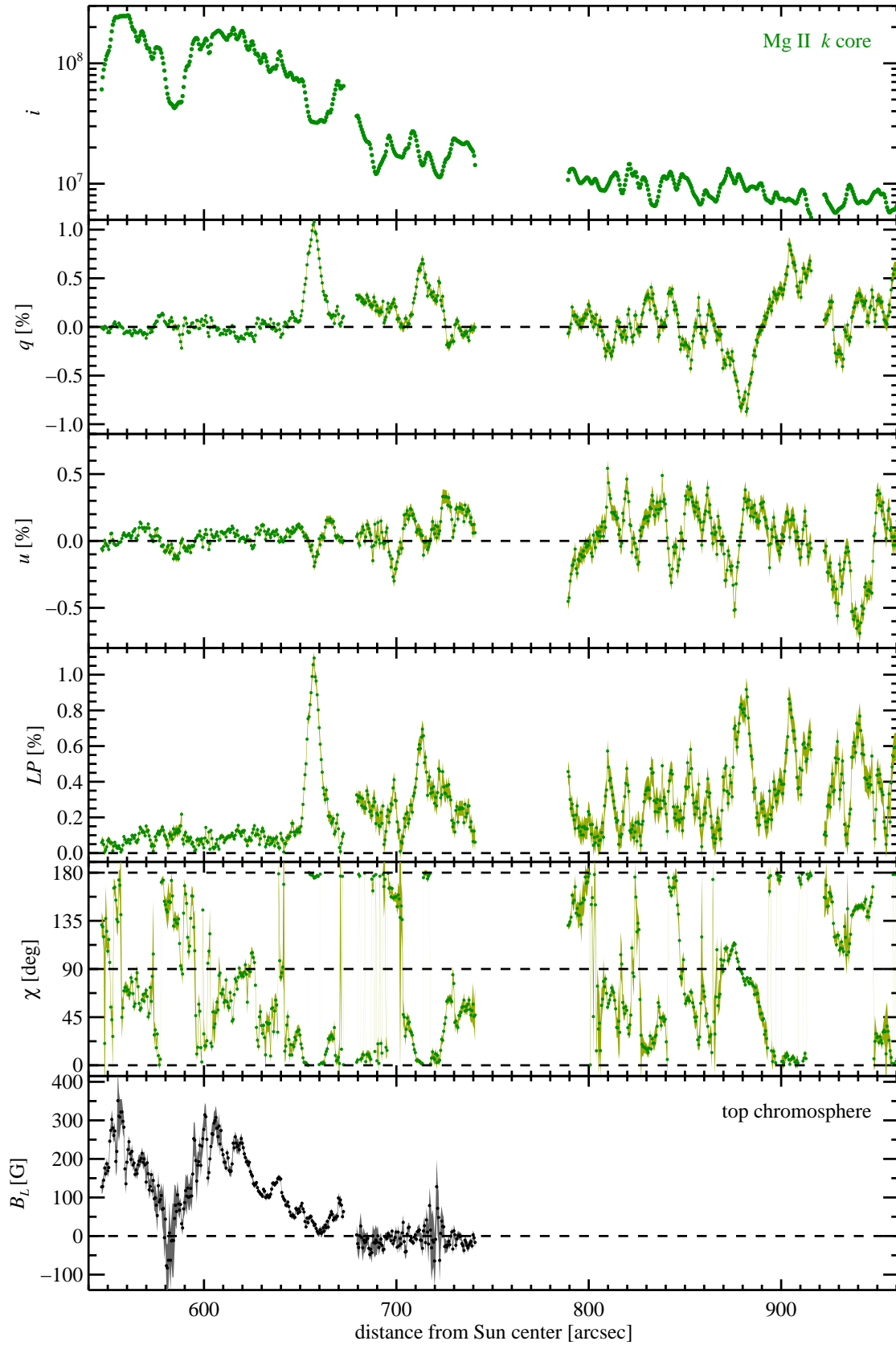
Figure 11. From top to bottom: spatial variations of i, q, u, LP, and χ at the core of the Mg II k line (the wavelength range indicated in green color in Fig. 3) and the longitudinal magnetic field $B_{\rm L}$ at the top of the chromosphere derived from the inner lobes of the Mg II h & k line. The shaded areas show the $\pm 1\sigma$ errors ($\pm\sigma_l$ for q, u, and LP, $\pm\sigma_\chi$ for χ, and $\pm\sigma_B$ for B_L).

Quiet Sun ($S = 601$ pix)						
	#i max	#pix of zero-cross	p	μ	σ	#u zero-cross
	n	s	s/S	np	$\sqrt{np(1-p)}$	
Mg II k core	30	86	0.14	4.2	1.9	10††
Near blue wing	31	101	0.17	5.2	2.1	9†
Near red wing	30	86	0.14	4.2	1.9	10††
Far blue wing	62	183	0.30	18.6	3.6	23†
Far red wing	59	210	0.34	20.1	3.6	34†††

Table 3. Number of i maxima (n), number of pixels with u zero-crossings (s), probability of a pixel being a u zero-crossing ($p = s/S$), expected number of u zero-crossing with local i maxima assuming the random distribution (μ) and the standard deviation (σ), and identified number of i maxima co-located with u zero-crossing (number of u zero-crossing points in Table 1) in the quiet region. In the rightmost column, the number of spatial coincidences between local i maxima and u zero-crossing that exceeds $\mu + \sigma$, $\mu + 2\sigma$, and $\mu + 3\sigma$ are indicated with †, ††, and † † †, respectively.

| Plage ($S = 330$ pix)						
	#i max	#pix of zero-cross	p	μ	σ	#u zero-cross
	n	s	s/S	np	$\sqrt{np(1-p)}$	
Mg II k core	24	51	0.15	3.6	1.7	5
Near blue wing	20	24	0.07	1.5	1.2	0*
Near red wing	26	50	0.15	3.9	1.8	4
Far blue wing	31	76	0.23	7	2.3	9
Far red wing	33	125	0.38	12.5	2.8	21††

Table 4. Same as Table 3, but in the plage region. In the rightmost column, the numbers of spatial coincidences between local i maxima and u zero-crossing that are smaller than $\mu - \sigma$ are indicated with ∗.
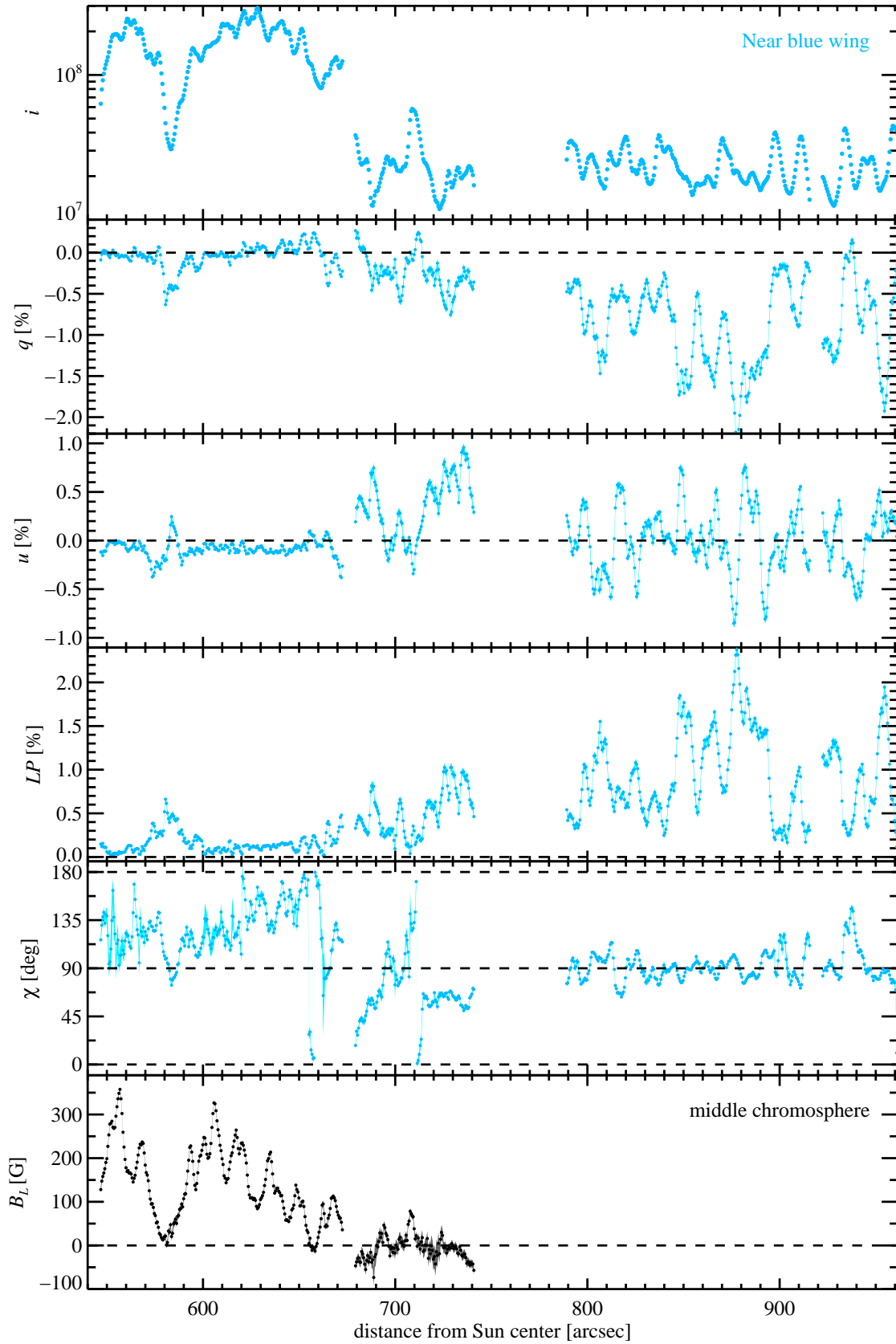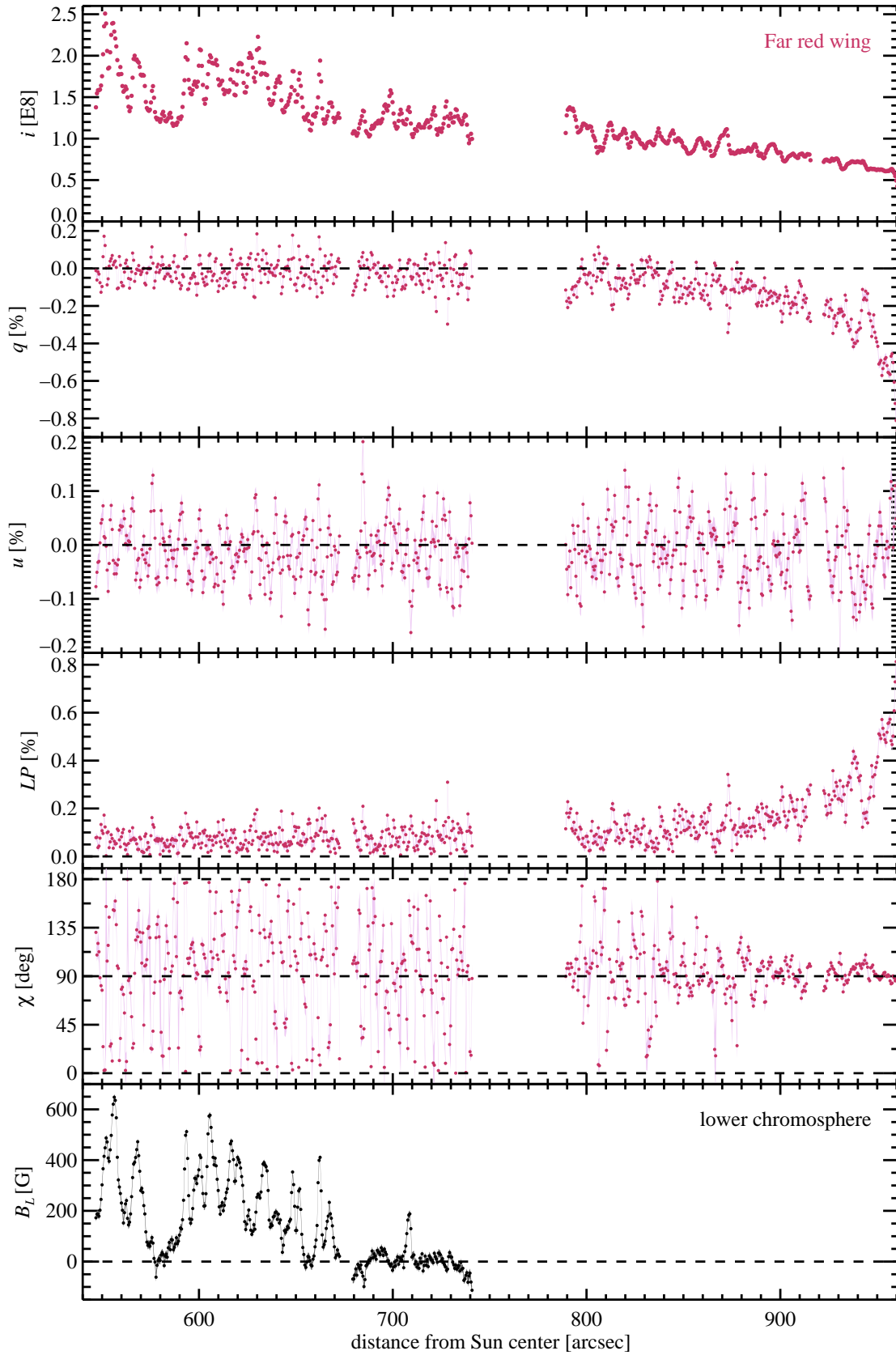
Figure 12. From top to bottom: spatial variations of i, q, u, LP, and χ at the near blue wing of the Mg II k line (the wavelength range indicated in light blue color in Fig. 3) and the longitudinal magnetic field B_L at the middle of the chromosphere derived from the external lobes of the Mg II h line. The shaded areas show the $\pm 1\sigma$ errors ($\pm \sigma_l$ for q, u, and LP, $\pm \sigma_\chi$ for χ, and $\pm \sigma_B$ for B_L).
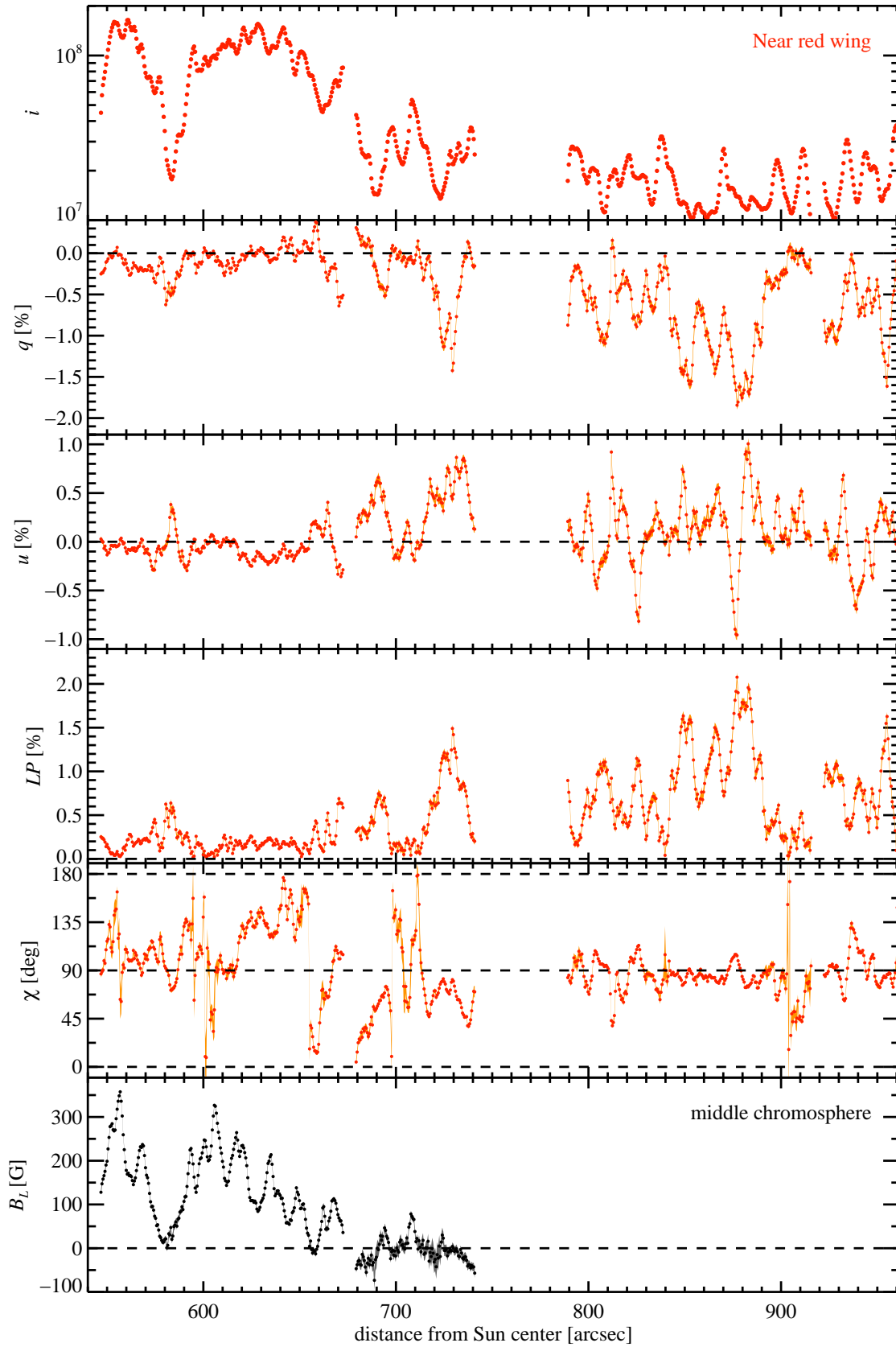
Figure 13. From top to bottom: spatial variations of i, q, u, LP, and χ at the near red wing of the Mg II k line (the wavelength range indicated in red color in Fig. 3) and the longitudinal magnetic field B_L at the middle of the chromosphere derived from the external lobes of the Mg II h line. The shaded areas show the $\pm 1\sigma$ errors ($\pm\sigma_l$ for q, u, and LP, $\pm\sigma_\chi$ for χ, and $\pm\sigma_B$ for B_L).
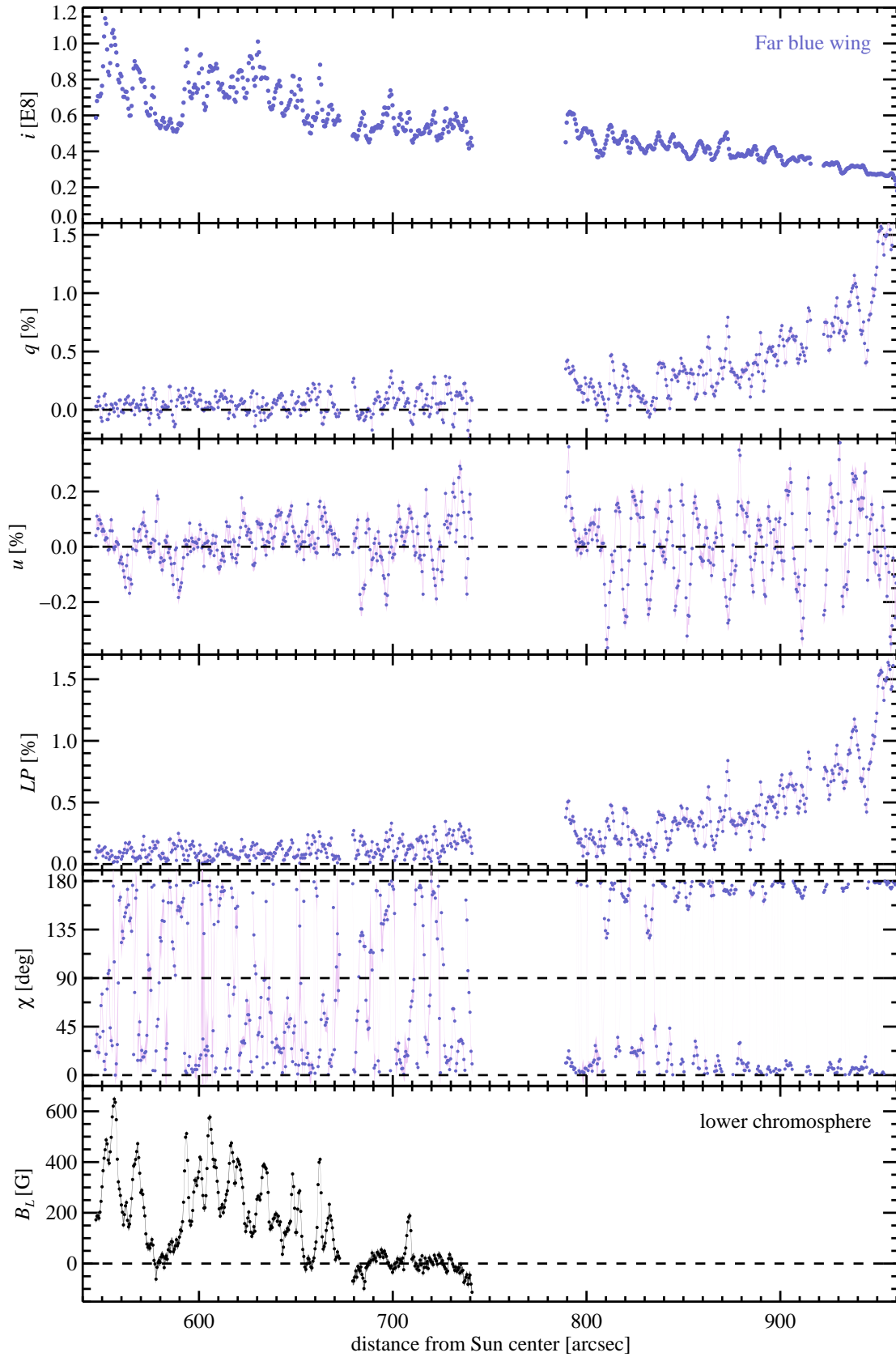
**Figure 14.** From top to bottom: spatial variations of i, q, u, LP, and χ at the far blue wing of the Mg II k line (the wavelength range indicated in violet color in Fig. 3) and the longitudinal magnetic field B_L at the bottom of the chromosphere derived from the Mn I lines. The shaded areas show the $\pm 1\sigma$ errors ($\pm\sigma_l$ for q, u, and LP, $\pm\sigma_\chi$ for χ, and $\pm\sigma_B$ for B_L).

Figure 15. From top to bottom: spatial variations of i, q, u, LP and χ at the far red wing of the Mg II k line (the wavelength range indicated in magenta color in Fig. 3) and the longitudinal magnetic field B_L at the bottom of the chromosphere derived from the Mn I lines. The shaded areas show the $\pm 1\sigma$ errors ($\pm\sigma_l$ for q, u, and LP, $\pm\sigma_\chi$ for χ, and $\pm\sigma_B$ for B_L).
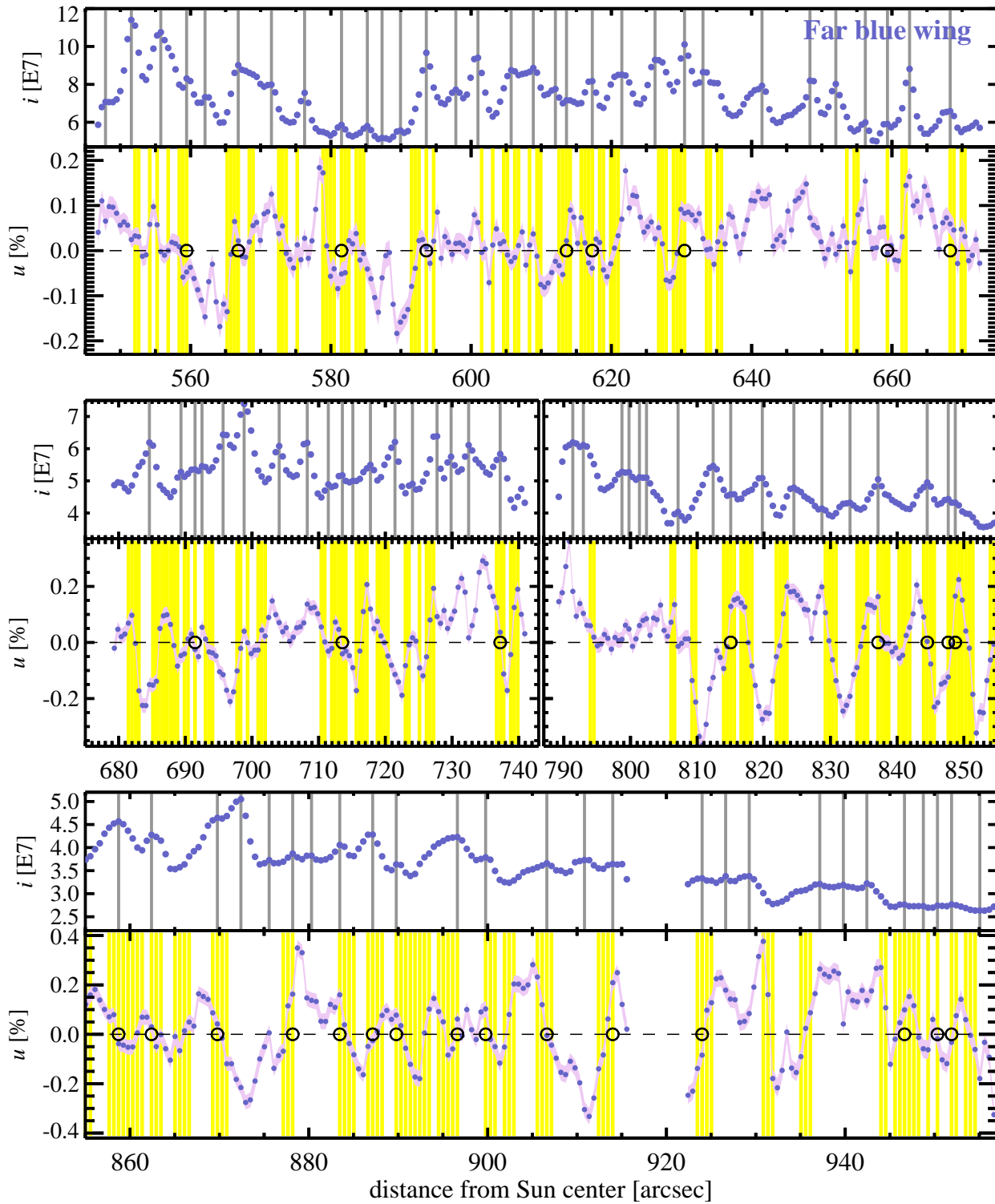
Figure 16. Same as Fig. 6, but for the far blue wing of the Mg II k line (see violet spectral range in Fig. 3).
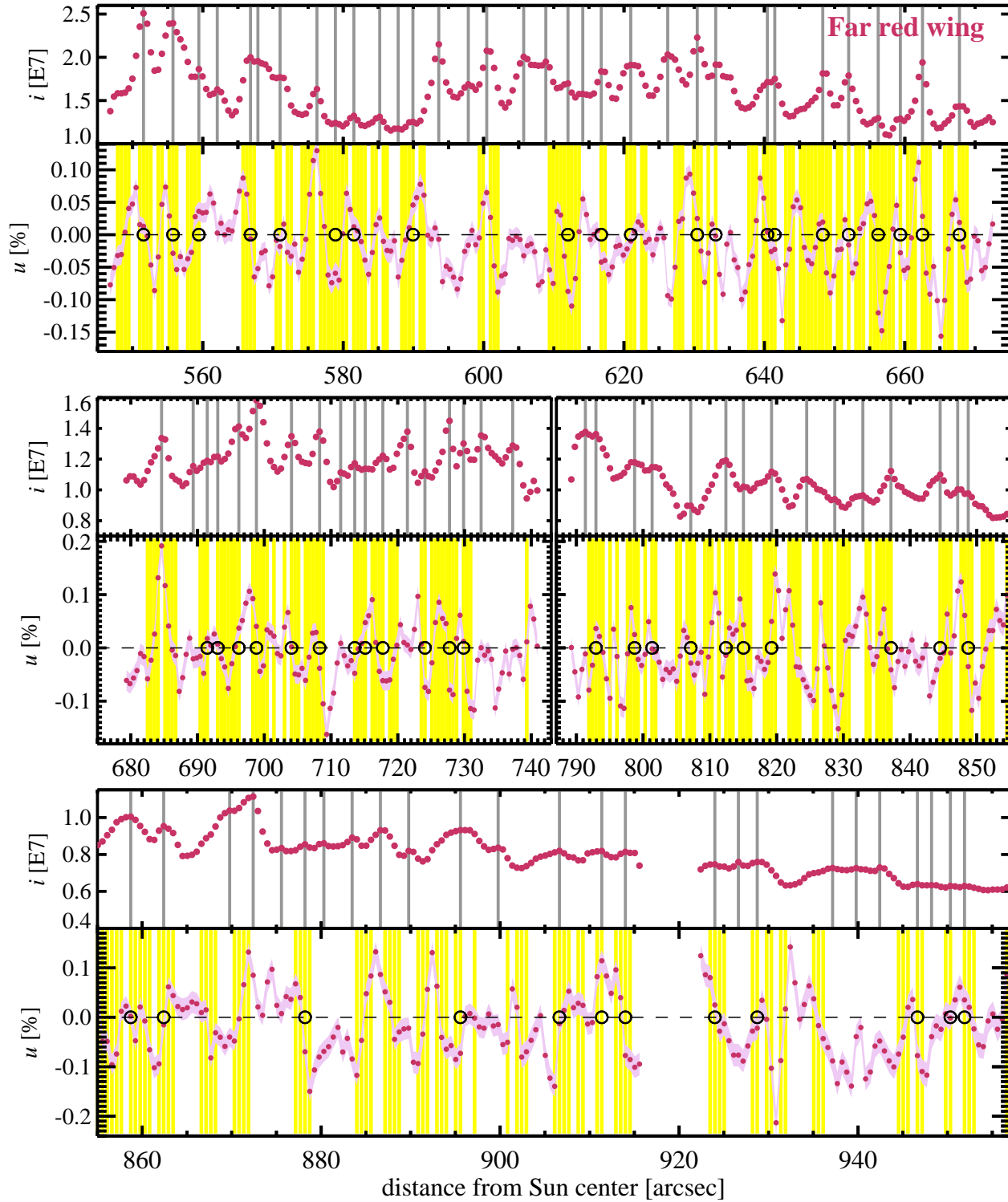
Figure 17. Same as Fig. 6, but for the far red wing of the Mg II k line (see magenta spectral range in Fig. 3).
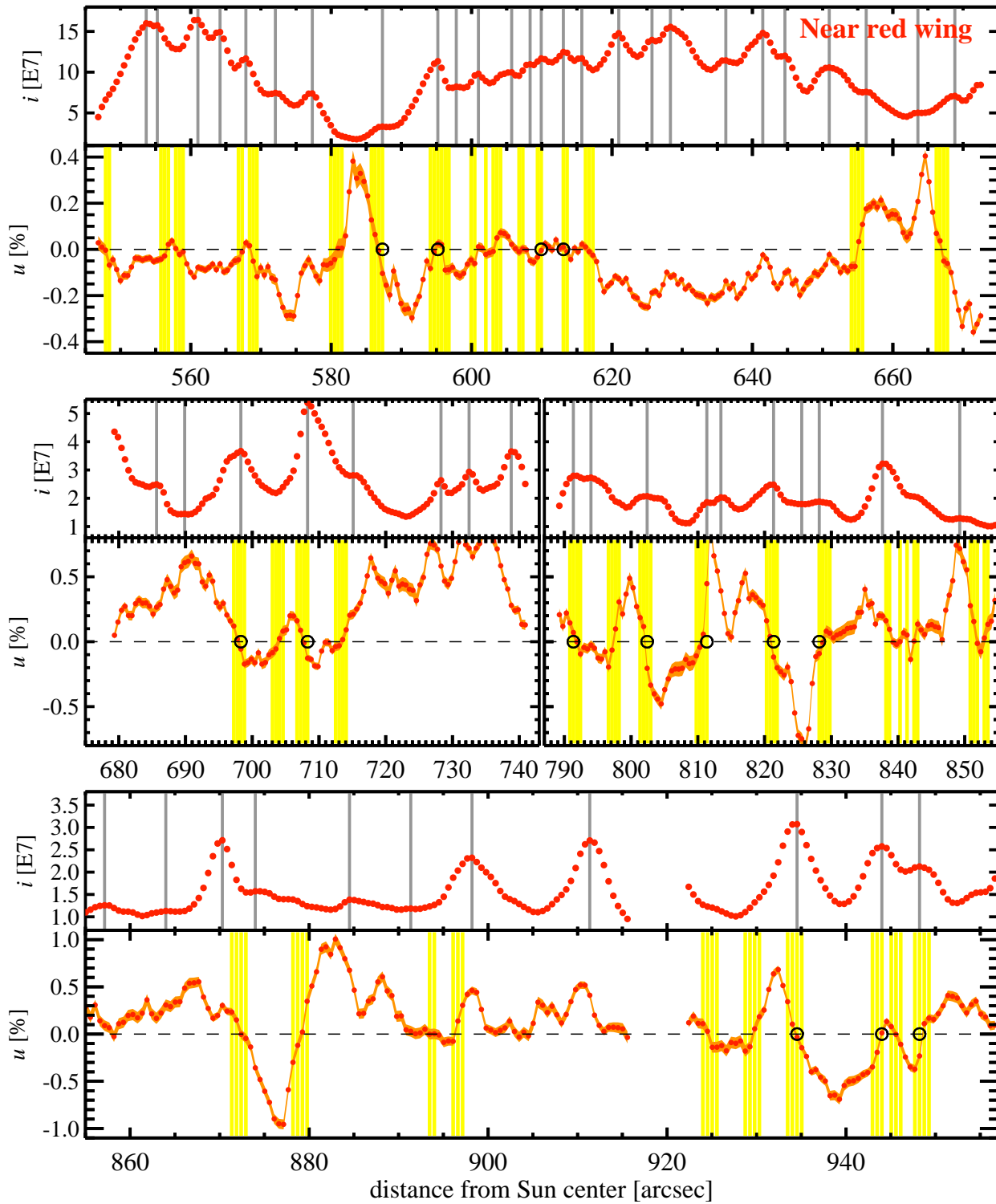
Figure 18. Same as Fig. 6, but for the near red wing of the Mg II *k* line (see red spectral range in Fig. 3).

Belluzzi, L., & Trujillo Bueno, J. 2012, ApJL, 750, L11, doi: 10.1088/2041-8205/750/1/L11

Carlin, E. S., Asensio Ramos, A., & Trujillo Bueno, J. 2013, ApJ, 764, 40, doi: 10.1088/0004-637X/764/1/40

del Pino Alemán, T., Alsina Ballester, E., & Trujillo Bueno, J. 2022, ApJ, 940, 78, doi: 10.3847/1538-4357/ac922c

del Pino Alemán, T., Casini, R., & Manso Sainz, R. 2016, ApJL, 830, L24, doi: 10.3847/2041-8205/830/2/L24

del Pino Alemán, T., Trujillo Bueno, J., Casini, R., & Manso Sainz, R. 2020, ApJ, 891, 91, doi: 10.3847/1538-4357/ab6bc9

Fontenla, J. M., Avrett, E. H., & Loeser, R. 1993, Astrophysical Journal, 406, 319

Ishikawa, R., Narukage, N., Kubo, M., et al. 2014, Solar Physics, 289, 4727

Ishikawa, R., Uitenbroek, H., Goto, M., Iida, Y., & Tsuneta, S. 2018, SoPh, 293, 74, doi: 10.1007/s11207-018-1293-6

Ishikawa, R., Kano, R., Bando, T., et al. 2013, ApOpt, 52, 8205, doi: 10.1364/AO.52.008205

Ishikawa, R., Trujillo Bueno, J., Uitenbroek, H., et al. 2017, ApJ, 841, 31, doi: 10.3847/1538-4357/aa6ca9

Ishikawa, R., Bueno, J. T., del Pino Alemán, T., et al. 2021, Science Advances, 7, eabe8406, doi: 10.1126/sciadv.abe8406

Ishikawa, S., Shimizu, T., Kano, R., et al. 2015, SoPh, 290, 3081, doi: 10.1007/s11207-015-0774-0

Jaume Bestard, J., Trujillo Bueno, J., Štěpán, J., & del Pino Alemán, T. 2021, ApJ, 909, 183, doi: 10.3847/1538-4357/abd94a

Kano, R., Trujillo Bueno, J., Winebarger, A., et al. 2017, ApJL, 839, L10, doi: 10.3847/2041-8213/aa697f

Kubo, M., Katsukawa, Y., Suematsu, Y., et al. 2016, ApJ, 832, 141, doi: 10.3847/0004-637X/832/2/141

Landi Degl'Innocenti, E., & Landolfi, M., eds. 2004, Astrophysics and Space Science Library, Vol. 307, Polarization in Spectral Lines

Lemen, J. R., Title, A. M., Akin, D. J., et al. 2012, SoPh, 275, 17, doi: 10.1007/s11207-011-9776-8

Li, H., del Pino Alemán, T., Trujillo Bueno, J., & Casini, R. 2022, ApJ, 933, 145, doi: 10.3847/1538-4357/ac745c

Manso Sainz, R., & Trujillo Bueno, J. 2011, ApJ, 743, 12, doi: 10.1088/0004-637X/743/1/12

Pesnell, W. D., Thompson, B. J., & Chamberlin, P. C. 2012, SoPh, 275, 3, doi: 10.1007/s11207-011-9841-3

Rachmeler, L. A., Bueno, J. T., McKenzie, D. E., et al. 2022, ApJ, 936, 67, doi: 10.3847/1538-4357/ac83b8

Song, D., Ishikawa, R., Kano, R., et al. 2018, in Society of Photo-Optical Instrumentation Engineers (SPIE) Conference Series, Vol. 10699, Space Telescopes and Instrumentation 2018: Ultraviolet to Gamma Ray, ed. J.-W. A. den Herder, S. Nikzad, & K. Nakazawa, 106992W, doi: 10.1117/12.2313056

Song, D., Ishikawa, R., Kano, R., et al. 2022, SoPh, 297, 135, doi: 10.1007/s11207-022-02064-8

Trujillo Bueno, J., Landi Degl'Innocenti, E., & Belluzzi, L. 2017, SSRv, 210, 183, doi: 10.1007/s11214-016-0306-8

Trujillo Bueno, J., Štěpán, J., & Casini, R. 2011, The Astrophysical Journal Letters, 738, L11

Trujillo Bueno, J., Štěpán, J., Belluzzi, L., et al. 2018, ApJL, 866, L15, doi: 10.3847/2041-8213/aae25a

Tsuzuki, T., Ishikawa, R., Kano, R., et al. 2020, in Society of Photo-Optical Instrumentation Engineers (SPIE) Conference Series, Vol. 11444, Society of Photo-Optical Instrumentation Engineers (SPIE) Conference Series, 114446W, doi: 10.1117/12.2562273

Štěpán, J., & Trujillo Bueno, J. 2012, in Astronomical Society of the Pacific Conference Series, Vol. 456, Fifth Hinode Science Meeting, ed. L. Golub, I. De Moortel, & T. Shimizu, 59. https://arxiv.org/abs/1205.2959

Štěpán, J., & Trujillo Bueno, J. 2016, ApJL, 826, L10, doi: 10.3847/2041-8205/826/1/L10

Štěpán, J., Trujillo Bueno, J., Leenaarts, J., & Carlsson, M. 2015, ApJ, 803, 65, doi: 10.1088/0004-637X/803/2/65

Yoshida, M., Song, D., Ishikawa, R., et al. 2018, in Society of Photo-Optical Instrumentation Engineers (SPIE) Conference Series, Vol. 10699, Space Telescopes and Instrumentation 2018: Ultraviolet to Gamma Ray, ed. J.-W. A. den Herder, S. Nikzad, & K. Nakazawa, 1069930, doi: 10.1117/12.2312463